

The Tarantula–Revealed by X-rays (T-ReX)

LEISA K. TOWNSLEY,^{1,*} PATRICK S. BROOS,¹ AND MATTHEW S. POVICH²

¹*Department of Astronomy & Astrophysics, 525 Davey Laboratory, Pennsylvania State University, University Park, PA 16802 USA*

²*Department of Physics & Astronomy, California State Polytechnic University, 3801 West Temple Ave, Pomona, CA 91768 USA*

Submitted to ApJS — 21 March 2024

ABSTRACT

The Tarantula Nebula (30 Doradus) is the most important star-forming complex in the Local Group, offering a microscope on starburst astrophysics. At its heart lies the exceptionally rich young stellar cluster R136, containing the most massive stars known. Stellar winds and supernovae have carved 30 Dor into an amazing display of arcs, pillars, and bubbles. We present first results and advanced data processing products from the 2-Ms *Chandra* X-ray Visionary Project, “The Tarantula – Revealed by X-rays” (T-ReX). The 3615 point sources in the T-ReX catalog include massive stars, compact objects, binaries, bright pre-main-sequence stars and compact young stellar (sub)clusters in 30 Dor. After removing point sources and excluding the exceptionally bright supernova remnant N157B (30 Dor B), the global diffuse X-ray maps reveal hot plasma structures resolved at 1–10 pc scales, with an absorption-corrected total-band (0.5–7 keV) X-ray luminosity of 2.110×10^{37} erg s⁻¹. Spatially-resolved spectral modeling provides evidence for emission lines enhanced by charge-exchange processes at the interfaces. We identify a candidate for the oldest X-ray pulsar detected to date in 30 Dor, PSR J0538-6902, inside a newly-resolved arctuate X-ray wind nebula, the Manta Ray. The long time baseline of T-ReX monitored dozens of massive stars, several showing periodic variability tied to binary orbital periods, and captured strong flares from at least three low-mass Galactic foreground stars.

Keywords: H II regions (694), High energy astrophysics (739), Early-type stars (430), Star formation (1569), Interstellar medium (847), Superbubbles (1656)

1. 30 DORADUS: A FIELD OF SUPERLATIVES

The Tarantula Nebula (30 Doradus, or 30 Dor), located in the Large Magellanic Cloud (LMC), is the most powerful massive star-forming region (MSFR) in the Local Group of galaxies. 30 Dor is

Corresponding author: Matthew S. Povich
mspovich@cpp.edu

* Deceased. This paper is part of a collection publishing posthumously the unfinished work of Leisa K. Townsley. Her coauthors completed the manuscript based on her initial draft, written notes and private communications.

unlike any Galactic MSFR; with no differential galactic rotation to rip the complex apart, it persists and grows at the confluence of two supergiant shells (Meaburn 1980) that have provided it with the fuel to power massive star formation for at least 25 Myr (Cignoni et al. 2015), reaching starburst proportions. Today it is dominated by its 1–2 Myr-old central massive cluster R136, containing the richest young stellar population in the Local Group, including the most massive stars known. Also in contrast to Galactic MSFRs, the location of 30 Dor in the LMC offers us a nearly face-on, low-metallicity starburst laboratory with low intervening absorption and a well-known distance. Pietrzyński et al. (2019) refined the distance to the LMC to 49.5 kpc, but we assume a 50 kpc distance to 30 Dor to facilitate comparison with other recent studies (e.g., Sabbi et al. 2013; Cheng et al. 2021; Chen et al. 2023). At this distance, the spatial scale is 0.24 pc/arcsec.

R136 produces ~ 1000 times the ionizing radiation of Orion (Conti et al. 2012) from at least five times as many early O-type stars as Carina (Evans et al. 2011). It contains several of the most massive stars known (Crowther et al. 2010) and the full complement of massive binaries, including WR–WR, WR–O, and O–O systems (Crowther & Dessart 1998). In the wider 30 Dor field, the presence of ~ 25 Myr-old evolved supergiants and embedded massive young stellar objects shows that 30 Dor is the product of multiple epochs of star formation (Walborn & Blades 1997; Whitney et al. 2008); the newest generation of embedded stars may represent triggered collapse from the effects of R136 (Walborn et al. 2013).

We present the 2 Ms *Chandra* X-ray Visionary Project, “The Tarantula—Revealed by X-rays” (T-ReX), an intensive imaging study of 30 Dor with the Advanced CCD Imaging Spectrometer (ACIS) instrument (Garmire et al. 2003) of the *Chandra X-ray Observatory*. Before T-ReX, *Chandra* had invested just 114 ks in this iconic target, revealing only the most massive stars and large-scale diffuse structures (Townasley et al. 2006a,b, 2014). T-ReX leverages the unparalleled X-ray spatial resolution of *Chandra*, a unique resource that will remain unmatched for another decade, revealing the X-ray properties of dozens of low-metallicity massive stars (see Crowther et al. 2022, hereafter C22) and parsec-scale shocks from winds and supernovae that are shredding its interstellar medium (ISM; the main science focus of this contribution, but see also Cheng et al. 2021; Chen et al. 2023). This definitive *Chandra* characterization of 30 Dor was motivated by the fundamental need to understand the complex machinery of a starburst. Massive stars, their remnants, and the lower-mass populations that accompany them exert a profound influence on dense molecular clouds through radiation and mechanical feedback, which both perpetuates and quenches star formation. T-ReX unveils the detailed spatial and spectral morphology of hot plasmas permeating the complex cold ISM structures, ionization fronts, and photon-dominated regions seen in optical and infrared (IR) images.

This paper is organized as follows: Section 2 describes the T-ReX observations and data processing, culminating in the publicly-available point-source catalog and other advanced data products. High-level descriptions and interpretation of the T-ReX images and point-source populations are presented in Sections 3 and 4, respectively. Section 5 presents our deeper dive into spatially-resolved spectral fitting analysis of the T-ReX diffuse emission and its physical properties. A brief summary of the anticipated legacy value of T-ReX is included in Section 6. Finally, two Appendices present more detailed analysis of select point-sources: Appendix A details the challenges of matching T-ReX point-sources to optical/IR source catalogs and presents tables of high-reliability matching results.

Appendix B presents light-curves and basic properties of notable X-ray variable sources, including massive stellar systems with periodic variability and low-mass stars exhibiting strong X-ray flares.

2. CHANDRA OBSERVATIONS AND DATA ANALYSIS

2.1. Observations

T-ReX obtained 51 *Chandra* imaging observations, using the 4 ACIS-I detectors plus the two central ACIS-S detectors, with an aimpoint near R136 over the period 2014 May 3 through 2016 January 22 (Table 1). The extreme ecliptic latitude (-87°) of 30 Dor limited T-ReX to 2 Ms due to spacecraft thermal constraints. Including three archival observations of 30 Dor from 2006 January brings the total exposure time to 2.05 Ms. The exposure map for all 54 observations, with detected point sources overlaid (see Section 2.3), is presented in Figure 1. Due to the various, arbitrary roll angles among the observations, the final exposure map resembles a daisy flower, with the two S-array detectors arranged like petals around a central disk created by rotating the four ACIS-I detectors. Both the greatest exposure time and on-axis point-source sensitivity are hence obtained within the central portions of ACIS-I (Figure 1b).

Table 1. Log of *Chandra* Observations

ObsID	Start Date	Exposure ^a	On-axis Position ^b		Roll	TGAIN ^c	Shift ^d
	(UT)	(s)	α_{J2000}	δ_{J2000}	($^\circ$)		(SKY pixel)
(1)	(2)	(3)	(4)	(5)	(6)	(7)	(8)
5906	2006-01-21	12317	05:38:43.92	-69:06:16.3	323	2005-11-01N6	(-0.285, -0.315)
7263	2006-01-22	42528	05:38:43.96	-69:06:16.4	323	2005-11-01N6	(-0.120, -0.254)
7264	2006-01-30	37593	05:38:43.54	-69:06:17.4	314	2005-11-01N6	(-0.076, -0.417)
16192	2014-05-03	93761	05:38:39.69	-69:06:28.1	222	2014-05-01N6_revA	(+0.305, -1.001)
16193	2014-05-08	75993	05:38:39.31	-69:06:26.8	218	2014-05-01N6_revA	(+0.119, -0.957)
16612	2014-05-11	22672	05:38:39.31	-69:06:26.8	218	2014-05-01N6_revA	(-0.048, -0.662)
16194	2014-05-12	31333	05:38:38.87	-69:06:24.9	212	2014-05-01N6_revA	(+0.480, -1.665)
16615	2014-05-15	45170	05:38:38.86	-69:06:25.0	212	2014-05-01N6_revA	(-0.193, -0.727)
16195	2014-05-24	44405	05:38:38.20	-69:06:21.4	202	2014-05-01N6_revA	(+0.928, -1.448)
16196	2014-05-30	67109	05:38:38.19	-69:06:21.4	202	2014-05-01N6_revA	(+0.323, -0.942)
16617	2014-05-31	58860	05:38:38.19	-69:06:21.3	202	2014-05-01N6_revA	(+1.063, -1.710)
16616	2014-06-03	34530	05:38:38.19	-69:06:21.3	202	2014-05-01N6_revA	(+0.008, -0.746)
16197	2014-06-06	67790	05:38:38.19	-69:06:21.3	202	2014-05-01N6_revA	(+0.911, -1.483)
16198	2014-06-11	39465	05:38:37.45	-69:06:14.9	187	2014-05-01N6_revA	(+1.397, -1.247)
16621	2014-06-14	44400	05:38:37.44	-69:06:14.9	187	2014-05-01N6_revA	(+1.211, -1.110)
16200	2014-06-26	27360	05:38:37.01	-69:06:06.8	170	2014-05-01N6_revA	(+1.720, -0.801)
16201	2014-07-21	58390	05:38:37.14	-69:05:54.0	145	2014-05-01N6_revA	(+0.158, -0.038)
16640	2014-07-24	61679	05:38:37.15	-69:05:54.0	145	2014-05-01N6_revA	(+0.594, -0.135)
16202	2014-08-19	65128	05:38:38.53	-69:05:41.8	117	2014-08-01N6_revA	(+0.561, +0.312)
17312	2014-08-22	44895	05:38:38.53	-69:05:41.8	117	2014-08-01N6_revA	(+0.481, +0.346)

Table 1 continued on next page

Table 1 (*continued*)

ObsID	Start Date	Exposure ^a	On-axis Position ^b		Roll	TGAIN ^c	Shift ^d
			α_{J2000}	δ_{J2000}			
(1)	(2)	(3)	(4)	(5)	(6)	(7)	(8)
16203	2014-09-02	41422	05:38:39.63	-69:05:37.4	102	2014-08-01N6_revA	(+0.243, +0.248)
17413	2014-09-08	24650	05:38:39.63	-69:05:37.3	102	2014-08-01N6_revA	(+0.718, +0.789)
17414	2014-09-13	17317	05:38:40.32	-69:05:35.5	94	2014-08-01N6_revA	(+0.356, -0.146)
16442	2014-10-25	48350	05:38:44.49	-69:05:35.6	50	2014-08-01N6_revA	(-0.138, -0.336)
17545	2014-10-28	34530	05:38:44.50	-69:05:35.5	50	2014-08-01N6_revA	(-0.071, -0.008)
17544	2014-11-01	25642	05:38:44.49	-69:05:35.7	50	2014-11-01N6	(+0.015, -0.032)
16443	2014-11-14	34530	05:38:45.51	-69:05:38.5	38	2014-11-01N6	(-0.014, +0.069)
17486	2014-12-04	33541	05:38:47.19	-69:05:48.3	12	2014-11-01N6	(+0.257, -0.702)
17555	2014-12-06	55246	05:38:47.18	-69:05:48.3	12	2014-11-01N6	(+0.557, -0.761)
17561	2014-12-20	54567	05:38:47.86	-69:05:58.9	350	2014-11-01N6	(+0.707, -0.514)
17562	2014-12-25	42031	05:38:47.85	-69:05:58.9	350	2014-11-01N6	(+0.602, -0.204)
16444	2014-12-27	41440	05:38:47.85	-69:05:58.9	350	2014-11-01N6	(+0.270, -0.188)
16448	2015-02-14	34599	05:38:46.12	-69:06:24.6	295	2015-02-01N6	(+0.722, -0.198)
17602	2015-02-19	51705	05:38:46.12	-69:06:24.5	295	2015-02-01N6	(+1.587, +0.330)
16447	2015-03-26	26868	05:38:43.31	-69:06:31.8	262	2015-02-01N6	(+0.243, +0.421)
16199	2015-03-27	39461	05:38:43.31	-69:06:31.9	262	2015-02-01N6	(+0.287, +0.669)
17640	2015-03-31	26318	05:38:43.31	-69:06:31.9	262	2015-02-01N6	(+0.326, +0.421)
17641	2015-04-04	24638	05:38:43.32	-69:06:31.9	262	2015-02-01N6	(+0.969, +1.656)
16445	2015-05-27	49310	05:38:37.81	-69:06:19.1	196	2015-05-01N6	(+0.286, +0.166)
17660	2015-05-29	38956	05:38:37.81	-69:06:19.1	196	2015-05-01N6	(-0.023, +0.124)
16446	2015-06-02	47547	05:38:37.68	-69:06:18.1	193	2015-05-01N6	(+0.117, +0.072)
17642	2015-06-08	34438	05:38:37.44	-69:06:15.6	188	2015-05-01N6	(+0.182, -0.065)
16449	2015-09-28	24628	05:38:41.66	-69:05:33.6	80	2015-08-01N6	(-1.468, -0.353)
18672	2015-11-08	30574	05:38:45.82	-69:05:39.8	34	2015-11-01N6	(-0.480, -1.424)
18706	2015-11-10	14776	05:38:45.80	-69:05:39.7	34	2015-11-01N6	(-0.889, -1.345)
18720	2015-12-02	9832	05:38:45.30	-69:05:58.0	357	2015-11-01N6	(-0.563, -1.301)
18721	2015-12-08	25598	05:38:44.95	-69:05:54.0	12	2015-11-01N6	(+0.040, -1.745)
17603	2015-12-09	13778	05:38:45.02	-69:05:55.1	8	2015-11-01N6	(+0.155, -1.927)
18722	2015-12-11	9826	05:38:45.16	-69:05:56.0	3	2015-11-01N6	(-0.510, -1.237)
18671	2015-12-13	25617	05:38:45.17	-69:05:56.1	3	2015-11-01N6	(-0.465, -1.112)
18729	2015-12-21	16742	05:38:45.18	-69:05:56.1	3	2015-11-01N6	(+0.500, -1.643)
18750	2016-01-20	48318	05:38:45.44	-69:06:07.5	324	2015-11-01N6	(+1.496, -0.875)
18670	2016-01-21	14565	05:38:45.43	-69:06:07.5	324	2015-11-01N6	(+0.905, -0.902)
18749	2016-01-22	22153	05:38:45.42	-69:06:07.4	324	2015-11-01N6	(+0.730, -1.058)

Table 1 *continued on next page*

Table 1 (*continued*)

ObsID	Start Date	Exposure ^a	On-axis Position ^b		Roll	TGAIN ^c	Shift ^d
	(UT)	(s)	α_{J2000}	δ_{J2000}	($^{\circ}$)		(SKY pixel)
(1)	(2)	(3)	(4)	(5)	(6)	(7)	(8)

- a Exposure times are the net usable times after various filtering steps are applied in the data reduction process. No exposure time needed to be removed during periods of high instrumental background. The time variability of the ACIS background is discussed in Section 6.16.3 of the *Chandra* Proposers' Observatory Guide (<http://asc.harvard.edu/proposer/POG/>) and in the ACIS Background Memos at http://asc.harvard.edu/cal/Acis/Cal_prods/bkgrnd/current/.
- b The On-axis Position is the time-averaged location of the optical axis (CIAO parameters RA_PNT,DEC_PNT) (<http://cxc.harvard.edu/ciao/faq/nomtargpnt.html>). Units of right ascension (α) are hours, minutes, and seconds; units of declination (δ) are degrees, arcminutes, and arcseconds.
- c Abbreviated name of the ACIS Time-Dependent Gain file used for calibration of event energies, e.g. "2002-02-01N6" = "acisD2002-02-01t_gainN0006.fits".
- d The shift (in RA and Dec) applied to the ObsID's aspect file (via the *CIAO* tool *wcs_update*) to achieve astrometric alignment, expressed as (dx,dy) in the *Chandra* "SKY" coordinate system (<http://asc.harvard.edu/ciao/ahelp/coords.html>); 1 SKY pixel = 0.492 arcsecond. Note that astrometric shifts are correlated in time.

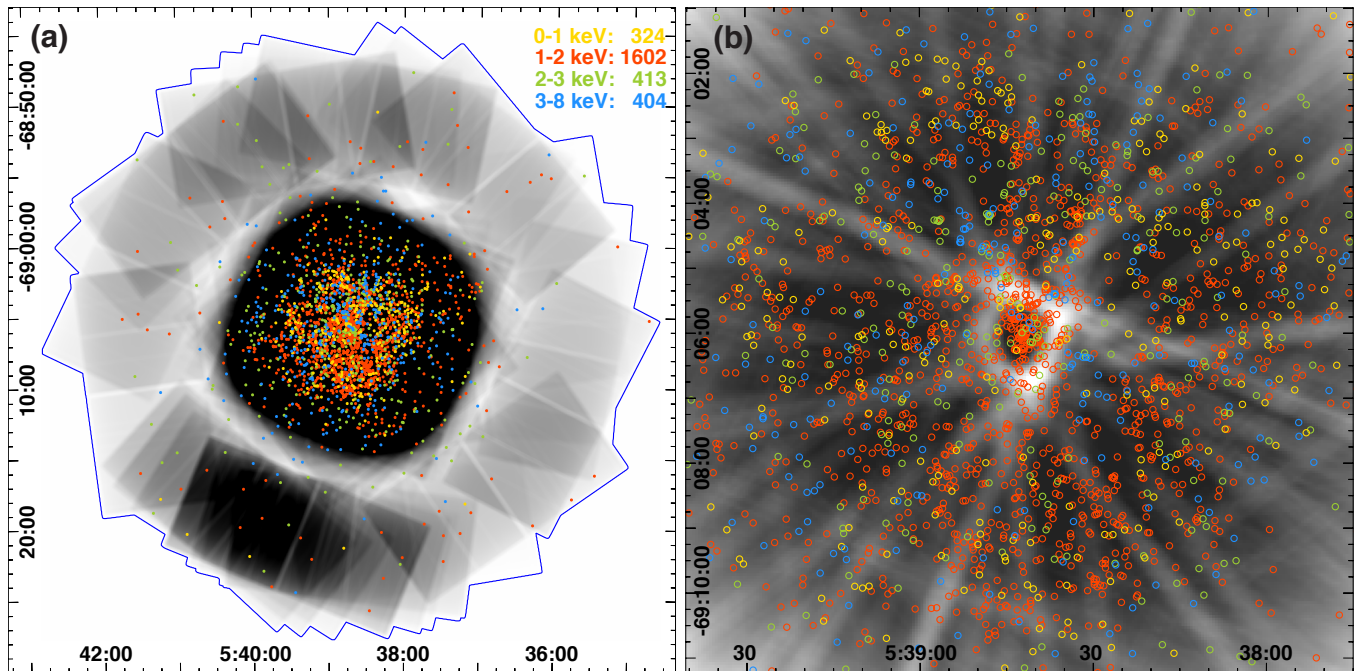


Figure 1. ACIS exposure map with 2743 brighter (≥ 5 net counts) ACIS point sources overlaid; colors denote median energy for each source. (a) The full T-ReX field. (b) A zoom of (a) showing the central $\sim 10'$ of the ACIS field.

2.2. Data Analysis

2.2.1. Methods, software, and procedures

The algorithms, procedures, and tools used for data reduction, astrometric alignment of observations, point source detection and validation, point source extraction, point source masking, construction of smoothed diffuse emission images, diffuse region extraction, and point source spectral fitting were the same as those used in MOXC2 and MOXC3 (Townsville et al. 2018, 2019). Please see those papers (and their references) for explanations of our data analysis methods. Even though all T-ReX observations have similar aimpoints, we followed our usual practice of extracting point sources and diffuse regions from each observation, and then combining those extractions and calibration products.

We employ a variety of standard and custom X-ray analysis software packages in our workflows. ACIS data are manipulated and calibrated using the *Chandra* data analysis system, *CIAO*¹ (Fruscione et al. 2006), and the *MARX*² observatory simulator (Davis et al. 2012). Throughout our workflow, data products are visually reviewed using the *SAOImage DS9*³ tool (Joye & Mandel 2003) and *TOPCAT*⁴ (Taylor 2005). Models are fit to extracted spectra using the *XSPEC*⁵ tool (Arnaud 1996). The algorithms and scripts driving these standard tools are implemented in the *ACIS Extract* (*AE*, Broos et al. 2010, 2012; Broos & Townsville 2016) software package⁶ and in a set of detailed procedures we developed. *AE* and most other custom software we use are written in the *Interactive Data Language*⁷ (IDL).

2.2.2. Alignment of Observations

When *Chandra* observations overlap, many data reduction tasks (e.g. source detection, position estimation, source extraction) are compromised if the misalignments among those observations are large (compared to the on-axis PSF). Thus, our standard data analysis includes iterative re-alignment of the observations to each other, and to an astrometric reference catalog. The astrometric reference catalog chosen for T-ReX consists of 20 sources⁸ from the VMC and 2MASS catalogs that are likely counterparts to bright and un-crowded X-ray sources observed less than 5' off-axis. The final shifts we applied to each observation, expressed in the *Chandra* SKY coordinate system⁹ are reported in Table 1. We estimate remaining misalignment among the ObsIDs to be approximately 0.02".

2.3. Point Source Catalog

Extraction apertures for the 3615 point sources in the T-ReX catalog are overlaid on an image of the full T-ReX event data in Figure 2. The catalog is published as an electronic table accompanying this article, and its columns are summarized in Table 2. The variation in both resolution and sensitivity as a function of increasing off-axis angle θ are evident in the aperture sizes (increasing) and point-source density (decreasing). Both event data and point-source density decrease further in the S-array detectors farther off-axis where the exposure time is unevenly reduced compared to the field center, due to arbitrary roll angles (Figure 1).

¹ <http://cxc.harvard.edu/ciao/>

² <http://space.mit.edu/ASC/marx>

³ <http://ds9.si.edu>

⁴ <http://www.star.bris.ac.uk/~mbt/topcat/>

⁵ <https://heasarc.gsfc.nasa.gov/xanadu/xspec/>

⁶ The *ACIS Extract* software package and User's Guide are publicly available from the Astrophysics Source Code Library, from Zenodo, and at http://personal.psu.edu/psb6/TARA/ae_users_guide.html.

⁷ www.harrisgeospatial.com/ProductsandTechnology/Software/IDL.aspx

⁸ X-ray sources p1_1194, p1_1234, p1_296, p1_1256, p1_1186, p1_611, p1_830, p1_995, p1_682, p1_1033, p1_441, p1_639, p1_450, p1_1391, p1_1317, p1_686 have likely counterparts in VMC. X-ray sources p1_711, p1_812, p1_911, p1_924 have likely counterparts in 2MASS.

⁹ <https://cxc.harvard.edu/ciao/ahelp/coords.html>

The extraction aperture for each observation of a point source is usually a contour of the local point spread function (PSF), chosen to enclose $\sim 90\%$ of the PSF for uncrowded observations or a reduced fraction to handle crowding (Broos et al. 2010). We manually increased aperture sizes for the following very bright sources: VFTS399 (Clark et al. 2015, source Label p1_610), Mk34 (Pollock et al. 2018, p1_995), R140a1/a2 (p1_752), Mk39 (p1_698), R144 (p1_1194), 053844.33-690554.7 (p1_1000), 053844.12-690556.6 (p1_979), SN1987A (c73). Two bright and severely crowded sources, R136a (p1_832) and R136c (p1_893), required hand-drawn apertures (see Fig. 1 of C22, and related discussion of these sources as blends of multiple unresolved massive stars.

Table 2. T-ReX X-ray Source Properties

Column Label (1)	Units (2)	Description (3)
Source identifiers		
Name	...	X-ray source name in IAU format; prefix is CXOU J
Label	...	X-ray source name used within the project ^a
Source position, derived from the set of ObsIDs that minimized position uncertainty (Broos et al. 2010, Section 6.2 and 7)		
RAdeg	deg	right ascension (ICRS) ^b
DEdeg	deg	declination (ICRS) ^b
PosErr	arcsec	1- σ error circle around (RAdeg,DEdeg)
PosType	...	algorithm used to estimate position (Broos et al. 2010, Section 7.1)
Validity metrics, derived from a pre-defined set of ObsID combinations (Townesley et al. 2018, Section 2.2.3)		
ProbNoSrc_MostValid	...	smallest of ProbNoSrc_t, ProbNoSrc_s, ProbNoSrc_h, ProbNoSrc_v (Broos et al. 2010, Section 4.3 and Weisskopf et al. 2007, Appendix A2) ^c
ProbNoSrc_t	...	smallest p -value under the no-source (0.5–7 keV) null hypothesis among validation merges
ProbNoSrc_s	...	smallest p -value under the no-source (0.5–2 keV) null hypothesis among validation merges
ProbNoSrc_h	...	smallest p -value under the no-source (2–7 keV) null hypothesis among validation merges
ProbNoSrc_v	...	smallest p -value under the no-source (4–7 keV) null hypothesis among validation merges
IsOccasional	boolean	flag indicating that source validation failed in all multi-ObsID merges; source validation comes from a single ObsID (Townesley et al. 2019, Section 3.1).
Variability indicators, derived from all ObsIDs		
ProbKS_single	...	$\min(P_1, P_2, \dots, P_{N_KS_single})$, where each P_i is the p -value arising from a Kolmogorov–Smirnov test of event arrive times under the null hypothesis of no variability within a single observation
N_KS_single	observations	number of p -values compared to produce ProbKS_single
ProbKS_merge	...	p -value from a Kolmogorov–Smirnov test on the combined events from all observations; the null hypothesis is no variability on any time scale
ProbChisq_PhotonFlux	...	p -value from a χ^2 test on the single-ObsID measurements of PhotonFlux_t; the null hypothesis is no inter-ObsID variability

Table 2 continued on next page

Table 2 (*continued*)

Column Label (1)	Units (2)	Description (3)
Observation details and photometric quantities, derived from all observations of the source		
ExposureTimeNominal	s	total exposure time in merged ObsIDs
ExposureFraction	...	fraction of ExposureTimeNominal that source was observed ^d
RateIn3x3Cell	count/frame	0.5:8 keV, in 3×3 CCD pixel cell ^e
NumObsIDs	observations	total number of ObsIDs extracted
NumMerged	observations	number of ObsIDs merged to estimate photometry properties
MergeBias	...	fraction of exposure discarded in merge
Theta.Lo	arcmin	smallest off-axis angle for merged ObsIDs
Theta	arcmin	average off-axis angle for merged ObsIDs
Theta.Hi	arcmin	largest off-axis angle for merged ObsIDs
PsfFraction	...	average PSF fraction (at 1.5 keV) for merged ObsIDs
SrcArea	(0.492 arcsec) ²	average aperture area for merged ObsIDs
AfterglowFraction	...	suspected afterglow fraction ^f
SrcCounts.t	count	observed counts (0.5–8 keV) in merged apertures
SrcCounts.s	count	observed counts (0.5–2 keV) in merged apertures
SrcCounts.h	count	observed counts (2–8 keV) in merged apertures
BkgScaling	...	scaling of the background extraction (Broos et al. 2010, Section 5.4)
BkgCounts.t	count	observed counts (0.5–8 keV) in merged background regions
BkgCounts.s	count	observed counts (0.5–2 keV) in merged background regions
BkgCounts.h	count	observed counts (2–8 keV) in merged background regions
NetCounts.t	count	net counts (0.5–8 keV) in merged apertures
NetCounts.s	count	net counts (0.5–2 keV) in merged apertures
NetCounts.h	count	net counts (2–8 keV) in merged apertures
NetCounts.Lo.t	count	1- σ lower bound on NetCounts.t ^g
NetCounts.Hi.t	count	1- σ upper bound on NetCounts.t ^g
NetCounts.Lo.s	count	1- σ lower bound on NetCounts.s ^g
NetCounts.Hi.s	count	1- σ upper bound on NetCounts.s ^g
NetCounts.Lo.h	count	1- σ lower bound on NetCounts.h ^g
NetCounts.Hi.h	count	1- σ upper bound on NetCounts.h ^g
MeanEffectiveArea.t	cm ² count photon ⁻¹	mean ARF value (0.5–8 keV) ^h
MeanEffectiveArea.s	cm ² count photon ⁻¹	mean ARF value (0.5–2 keV) ^h
MeanEffectiveArea.h	cm ² count photon ⁻¹	mean ARF value (2–8 keV) ^h
MedianEnergy.t	keV	median energy, observed spectrum (0.5–8 keV) ⁱ
MedianEnergy.s	keV	median energy, observed spectrum (0.5–2 keV) ⁱ
MedianEnergy.h	keV	median energy, observed spectrum (2–8 keV) ⁱ
PhotonFlux.t	photon cm ⁻² s ⁻¹	apparent photon flux (0.5–8 keV) ^j
PhotonFlux.s	photon cm ⁻² s ⁻¹	apparent photon flux (0.5–2 keV) ^j
PhotonFlux.h	photon cm ⁻² s ⁻¹	apparent photon flux (2–8 keV) ^j
EnergyFlux.t	erg cm ⁻² s ⁻¹	max(EnergyFlux.s,0) + max(EnergyFlux.h,0)
EnergyFlux.s	erg cm ⁻² s ⁻¹	apparent energy flux (0.5–2 keV) ^j
EnergyFlux.h	erg cm ⁻² s ⁻¹	apparent energy flux (0.5–2 keV) ^j

Table 2 *continued on next page*

Table 2 (*continued*)

Column Label	Units	Description
(1)	(2)	(3)

NOTE— These X-ray columns are produced by the *ACIS Extract* (*AE*, Broos et al. 2010, 2012; Broos & Townsley 2016) software package. Similar column labels were previously published by the CCCP (Broos et al. 2011), MOXC1, MOXC2, and MOXC3. *AE* and its User’s Guide are publicly available from the Astrophysics Source Code Library, from Zenodo, and at http://personal.psu.edu/psb6/TARA/ae_users_guide.html.

^aSource “labels” identify each source during data analysis, as the source position (and thus the Name) is subject to change.

^bACIS ObsIDs are shifted to align with our astrometric reference catalog, composed of 20 stars chosen from the VISTA Magellanic Survey (Cioni et al. 2011, VMC) and Two Micron All Sky Survey (2MASS, Skrutskie et al. 2006).

^cThe suffixes “_t”, “_s”, “_h”, and “_v” on source validation *p*-values (“ProbNoSrc_*”) designate the 0.5–7 keV, 0.5–2 keV, 2–7 keV, and 4–7 keV energy bands.

^dDue to dithering over inactive portions of the focal plane, a *Chandra* source often is not observed during some fraction of the nominal exposure time (<http://cxc.harvard.edu/ciao/why/dither.html>). We report here the *CIAO* quantity “FRACEXPO” produced by the tool *mkarf*.

^eSource properties in this table are *not* corrected for pile-up effects. RateIn3x3Cell is an estimate of the observed count rate falling on an event detection cell of size 3×3 ACIS pixels, centered on the source position. When RateIn3x3Cell > 0.05 (count/frame), the reported source properties may be biased by pile-up effects. See Section 2.6 for a list of source extractions confirmed to have significant pile-up.

^fSome background events arising from an instrumental effect known as “afterglow” (<http://cxc.harvard.edu/ciao/why/afterglow.html>) may contaminate source extractions. After extraction, we attempt to identify afterglow events using the *AE* tool *ae_afterglow_report*, and report the fraction of extracted events attributed to afterglow; see the *AE* manual.

^gConfidence intervals (68%) for NetCounts quantities are estimated by the *CIAO* tool *aprates* (<http://asc.harvard.edu/ciao/ahelp/aprates.html>).

^hThe Ancillary Response File (ARF) in ACIS data analysis represents both the effective area of the Observatory and the fraction of the observation time for which data were actually collected for the source (column ExposureFraction).

ⁱMedianEnergy is the median energy of extracted events, corrected for background but dependent on the shape of the Effective Area curves for the extractions of the source (Broos et al. 2010, Section 7.3).

^jPhotonFlux = (NetCounts / MeanEffectiveArea / ExposureTimeNominal) (Broos et al. 2010, Section 7.4). EnergyFlux = 1.602 × 10^{−9}(erg/keV) × PhotonFlux × MedianEnergy (Getman et al. 2010, Section 2.2). Because MeanEffectiveArea depends on the shape of the Effective Area curves for the extractions of the source, PhotonFlux and EnergyFlux exhibit source-dependent calibration errors.

Source identifiers and position quantities (Name, RAdeg, DEdeg, PosErr, PosType) are computed using a subset of extractions for each source chosen to minimize the position uncertainty (Broos et al. 2010, Section 6.2 and 7.1). Source significance quantities in each energy band (ProbNoSrc_*) are computed using a pre-defined set of ObsID combinations which do not depend on the data observed (Townsley et al. 2018, Section 2.2.3). Because T-ReX observations have similar aimpoints, source significance ends up being calculated for each individual observation and for the combination of all observations. Source detection used our standard significance threshold (<1% chance that the source is a random background fluctuation in the combination of extraction and energy band generating the highest detection significance), corresponding to ProbNoSrc_MostValid < 0.01. Of course, identifying a multiwavelength counterpart to a faint X-ray point source (Appendix A) generally increases confidence that the detection is an astrophysical object.

Variability indices (ProbKS_single, ProbKS_merge, and ProbChisq_PhotonFlux; see Section 2.5 below) are computed using all observations. Quantities in the remaining columns of Table 2 are computed using a subset of ObsIDs, chosen independently for each source, to balance the conflicting

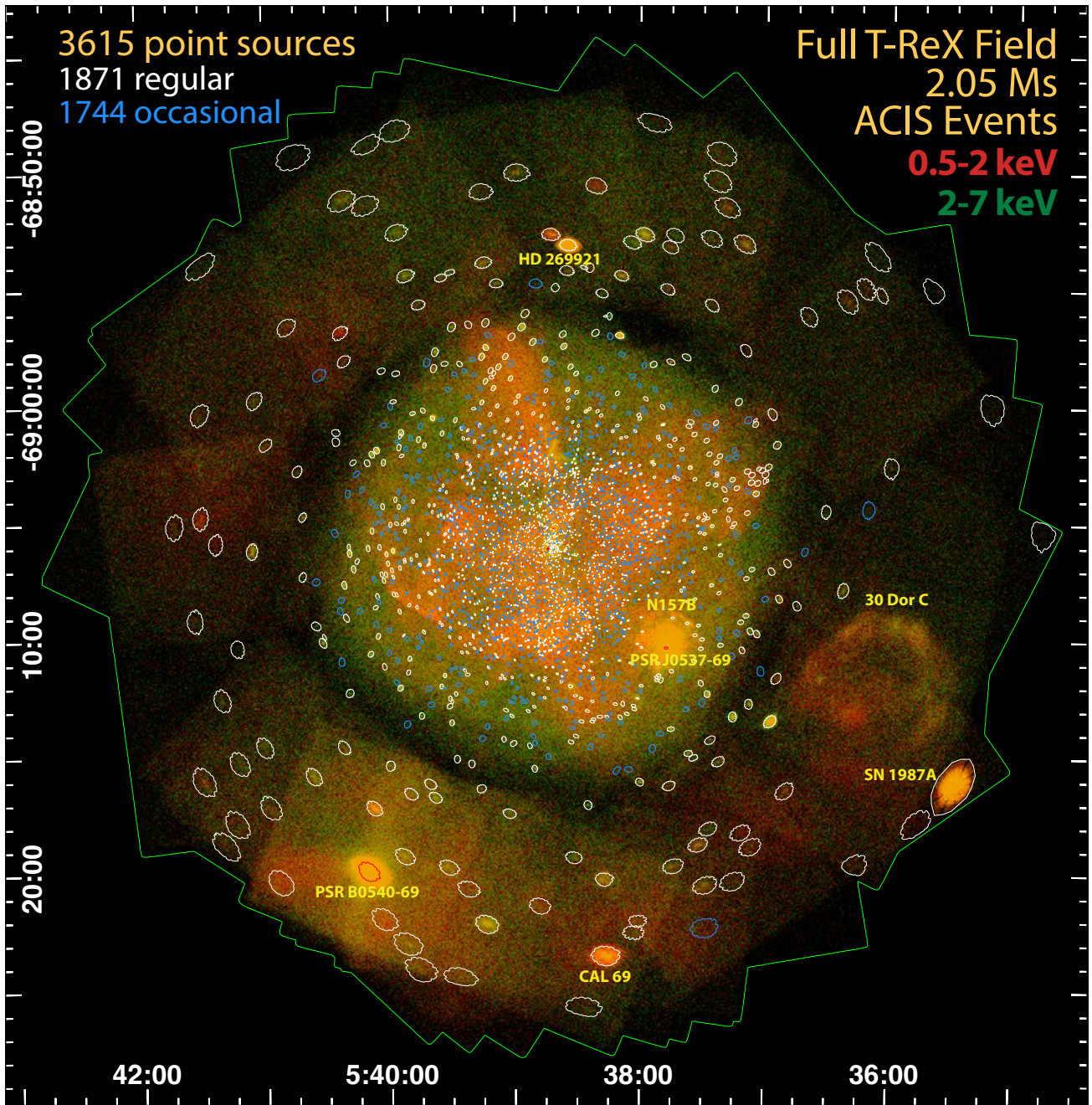


Figure 2. The T-ReX event data for the full T-ReX field. Events are binned by 4 sky pixels ($2''$). Soft events (0.5–2 keV) are shown in red, hard events (2–7 keV) in green. Regular point sources are outlined by blue polygons, “occasional” sources by white polygons. Red polygons outline sources exhibiting significant pile-up. These polygons are examples of event extraction regions, usually based on 90% encircled energy PSF contours. Notable off-axis sources discussed in the text are labeled in yellow.

goals of minimizing photometric uncertainty and of avoiding photometric bias (Broos et al. 2010, Section 6.2 and 7).

As with many ACIS studies, the (up to 54) extractions of a specific source in T-ReX do not share identical calibrations. Even observations taken on the same CCD detector in the same configuration

suffer from time-dependent Effective Area curves due to time-varying contamination on the [ACIS Optical Blocking Filters](#)¹⁰. These calibration variations among source extractions introduce biases into certain uncalibrated source properties (e.g., `MedianEnergy_*`) and introduce source-dependent calibration errors into other source properties (e.g., `PhotonFlux`, `EnergyFlux`, `ProbKS_merge`, and `ProbChisq_PhotonFlux`). Spectral fitting is needed to account for these calibration differences and to establish actual flux changes in sources that might be variable.

2.4. Sources Flagged as “Occasional”

Nearly half ($1744/3615 = 48\%$) of sources in the catalog have the Boolean flag `IsOccasional` set (Table 2); these sources are also identified in Figure 2 and subsequent figures displaying point sources overlaid on various images. The “occasional” flag, defined in [Townesley et al. \(2019, MOXC3; Section 3.1\)](#), is set when “source validation failed in all attempted multi-ObsID extraction combinations, but succeeded in one or more single-ObsID extractions.” Since T-ReX observations have similar aimpoints, occasional sources are those that failed validation when all observations were combined, but passed validation in one or more single-ObsID extractions. By contrast, we denote sources validated in multi-ObsID extractions as “regular.”

In the MOXC3 catalog, 14% of sources were flagged as occasional, a much lower fraction than in T-ReX. But T-ReX differs from our previous MOXC catalogs in the large number of ObsIDs targeting a single area on the sky, which increases the chances that a spurious source could be valid in a given single ObsID. This probably explains the much larger fraction of occasional sources in T-ReX.

It is important to emphasize that flagging a source `IsOccasional` is *not* a claim of variability, indeed, as [Townesley et al. \(2019\)](#) noted, most occasional sources are too faint to assess X-ray variability. The majority of occasional sources in the T-ReX catalog have $\lesssim 12$ `NetCounts_t`, while the large majority of regular sources exceed this value. Occasional sources also appear marginally softer than regular sources (e.g., in the `MedianEnergy_t` distributions). As a test, we stacked the spectra of occasional sources in T-ReX and found that their total (gross) spectrum, local background spectrum, and net spectrum look very similar to each other and similar to the gross global diffuse spectrum (Section 5). It is hence plausible that many occasional sources could be knots of diffuse emission, but they could also include faint astrophysical sources at the detection limit.

We choose to include occasional sources in the catalog because (1) some of them may represent real X-ray counterparts to astrophysical objects detected at other wavelengths, and (2) they are subject to the source masking process in our diffuse emission work flow. We hence regard the 1871 “regular” sources as the more-reliable subset of the T-ReX catalog and those with the “occasional” property as a more complete set of candidate point sources.

2.5. Variability Metrics

The point source catalog (Table 2) reports information that can help identify source variability on two timescales. Short-term variability is assessed within each observation of a source. *AE* calculates a *p*-value for the observed arrival times of extracted (point source + background) in-band events from that observation, under the null hypothesis of a constant event rate, using a one-sample Kolmogorov-Smirnov (K-S) hypothesis test ([Broos et al. 2010, Section 7.6](#)). If we reported all of those *p*-values (up to 54 in T-ReX), then variable sources within a *specific* observation could be identified by applying

¹⁰ <http://cxc.harvard.edu/ciao/why/acisquecontamN0010.html>

a threshold to the p -values from that observation. However, observers are more typically interested in sources that show evidence for variability in *any* of the observations. This is a classic [multiple comparisons problem](#)¹¹, wherein any one of multiple observations can produce the “discovery” of short-term variability.

Every extraction that produces four or more X-ray events is tested for variability. Instead of reporting p -values from each of those tests, we choose to report the smallest p -value produced by each source, as `ProbKS_single` in Table 2. Note that the statistic `ProbKS_single` = $\min(P_1, P_2, \dots, P_{N_{\text{KS_single}}})$ is *not* uniformly distributed under the null hypothesis, and is thus *not* a p -value. However, a proper p -value can be calculated via

$$p = 1 - (1 - \text{ProbKS_single})^{N_{\text{KS_single}}}. \quad (1)$$

If a set of N sources is screened for variability by thresholding this p -value (e.g. “variable” $\Leftrightarrow p < 0.005$), then the number of false positives expected would be approximately N multiplied by the threshold (e.g. $N \times 0.005$).¹² This intra-ObsID variability testing requires no calibration information, because instrument response is not expected to vary during an observation.

To assess variability over longer timescales than a single exposure (typically 15–60 ks, Table 1) one must consider all observations of a source. We assess Inter-ObsID variability using a K–S test (`ProbKS_merge`) that combines all the observations of the source (Broos et al. 2010, Section 7.6) and also by employing a standard χ^2 test (`ProbChisq_PhotonFlux`) on the single-ObsID measurements of `PhotonFlux_t`. Computation of both metrics requires calibration information. The instrument response for a given source will always vary across observations, due to both chromatic effects (aperture correction, mirror response, ACIS Optical Blocking Filter transmission, CCD response) and achromatic effects (dead time, exposure lost to inactive CCD pixels). The combined energy-dependent effect of these calibration factors is represented by the Ancillary Response File (ARF) calculated for each source extraction. For all multi-ObsID projects, the accuracy of the two long-term variability metrics produced by *AE* (`ProbKS_merge` and `ProbChisq_PhotonFlux`) is limited by their assumption that the single-ObsID ARFs have the same *shape* (i.e. differ only in normalization). In T-ReX the calibration factor that most strongly invalidates this assumption is the time-dependent variation in the ACIS Optical Blocking Filter transmission.

Thus in T-ReX and many previous projects (Broos et al. 2011; Townsley et al. 2014, 2018, 2019) thresholding `ProbKS_merge` or `ProbChisq_PhotonFlux` should be viewed as a *screening* test for possible variability, rather than as a calibrated null hypothesis test using an accurate p -value; false-positives are expected. The only accurate method for measuring source variability across all observations would be simultaneous fitting of all single-ObsID spectra, which is beyond the scope of this paper.

We do not attempt to flag all candidate variable sources in the T-ReX point source catalog, but in Appendix B we discuss seven examples of high-quality periodic X-ray variables and two large X-ray flares associated with foreground Galactic stars in the T-ReX field.

¹¹ https://en.wikipedia.org/wiki/Multiple_comparisons_problem

¹² If instead variability were determined by thresholding the statistic `ProbKS_single` (e.g. “variable” $\Leftrightarrow \text{ProbKS_single} < 0.005$), then the number of false positives expected would be approximately the total number of K–S tests performed in that set of sources, multiplied by the threshold (e.g. $\sum_{i=1}^N N_{\text{KS_single}_i} \times 0.005$). Such an approach would produce a much higher false-positive rate for variability, given the large number of ObsIDs in T-ReX.

2.6. Sources Suffering Photon Pile-up

Three point sources (Mk34, R140a, PSR J0537-6910) have extractions that are significantly impacted by an instrumental non-linearity known as *photon pile-up*¹³, which is described in the three MOXC papers (Townsville et al. 2014, 2018, 2019, and references therein). When possible, we model the piled-up spectra in these extractions (Broos et al. 2011) and use that model to estimate a “reconstructed” ACIS spectrum free from pile-up effects. The metric we choose to describe the severity of pile-up is the ratio of the pile-up-free count rate to the observed (piled-up) count rate in the total (0.5–8 keV) energy band, which we call the Rate Correction.

Rate Corrections for the colliding-wind Wolf-Rayet binary system Mk34 (053844.25-690605.9 = p1_995, VFTS 770) range from 1.176 when the count rate was highest (ObsID 17312) to 1.0 (no pile-up) when the count rate was lowest. Pollock et al. (2018, Figure 6) compare spectral fits to the piled and corrected spectra.

The nearly constant colliding-wind Wolf-Rayet binary system R140a (053841.59-690513.4 = p1_752, see C22) produced moderate Rate Corrections (~ 1.07) in all observations.

Although the pulsar PSR J0537-6910 (053747.40-691020.2 = p1_255) has count rates about 5 times larger than Mk34 and R140a, it has similarly moderate Rate Corrections because its photons were distributed over a much larger PSF (6′ off-axis).

2.7. Archive of Reduced Data Products

The Zenodo archive [10.5281/zenodo.8388113](https://zenodo.org/record/8388113)¹⁴ (Townsville & Broos 2023) contains data products and plots that may be of use to other investigators who wish to use the T-ReX data set; see the file README.TXT there for details.

3. AN IMAGING TOUR OF T-REX

To emphasize various morphological features of the T-ReX diffuse X-ray emission, we present in this section several visualizations of the imaging data with no overlays. Soft diffuse emission, divided into three energy bands, across the full T-ReX field is shown in Figure 3. This field is 40′ \approx 580 pc in diameter. The image has been smoothed to achieve a roughly constant SNR and showcases the dramatic improvement in spatial resolution afforded by the increased SNR of the 2 Ms T-ReX exposure compared to previously published images (Townsville et al. 2006a, 2011c).

Based on earlier, shallower and hence blurrier images, 30 Dor appeared to exhibit at least five plasma-filled superbubbles (Townsville et al. 2006a), products of strong OB winds and multiple supernovae. Because of their proximity and the low absorbing column to the LMC, they provide the best opportunity to study the X-ray spectrum and structure of any superbubble system. *Chandra* has already shown (Townsville et al. 2011c; Lopez et al. 2011; Pellegrini et al. 2011) that they are spatially complex X-ray structures with a range of X-ray plasma temperatures, ionization timescales, absorptions, and luminosities. The T-ReX images reveal that the ISM in 30 Dor, as in Carina and other MSFRs, forms a complex labyrinth of low-density cells and channels filled with hot plasma, surrounded by walls of colder material. The boundaries apparently separating the superbubble lobes are much less distinct in the deeper observations that more effectively penetrate absorbing columns of the cold, dense ISM walls, shells, and filaments.

¹³ http://cxc.harvard.edu/ciao/why/pileup_intro.html

¹⁴ <https://zenodo.org/record/8388113>

The outer regions of the T-ReX field are suffused with fainter, softer (red-green in in Figure 3) emission that also shows rich spatial structure. Much of this spatial complexity could be explained by the imprint of spatially-varying absorption (see Figure 4) on background of X-ray emission that is intrinsically softer than 30 Dor itself. Some of this emission could be hot plasma leaking from the 30 Dor superbubbles.

Three neighboring structures, labeled in Figure 2, stand out in the 1.1–2.3 keV band against the softer background. The ~ 5 -Myr-old star-forming region NGC 2060 (Sabbi et al. 2016), located $\sim 6'$ southwest of R136, is dominated by the young SNR N157B (also known as 30 Dor B), containing the 16-ms PSR J0537-6910, the most energetic pulsar known (Chen et al. 2006, 2023). N157B and its prominent cometary pulsar wind nebula contributed over half of the total X-ray counts in prior *Chandra* studies of 30 Dor (Townesley et al. 2006a). West of N157B lies the 30 Dor C superbubble, a large shell of non-thermal X-ray emission, which appears as an elongated, broken blue ring surrounding (in projection) a compact, softer source that has been identified as MCSNR J0536–6913 (Kavanagh et al. 2015). A hard-edged artifact produced by smoothing over the mask for the exceptionally bright PSR B0540-69 appears in the S-array mosaic SE of 30 Dor. Enhanced hard diffuse emission in the vicinity is likely associated with the young, oxygen-rich SNR reported by Park et al. (2010) using on-axis *Chandra* observations.

In Figures 4 and 5 we highlight the complex morphological interplay between the hot X-ray emitting plasma, and the cool, dusty ISM revealed in *Spitzer* images.¹⁵ In these images, the *Spitzer*/IRAC 8 μm band (green) shows primarily emission from polycyclic aromatic hydrocarbons (PAHs) that produce a strong 7.7 μm fluorescence feature when exposed to UV irradiation (Povich et al. 2007), making it an excellent tracer of locations where the surfaces of cold, molecular clouds are exposed to ionizing radiation. The *Spitzer*/MIPS 24 μm band (red) traces warm dust, which emits most strongly where dust grains are intermixed with ionized plasma and becomes stochastically heated by the hard radiation field (Watson et al. 2008; Everett & Churchwell 2010). The full ACIS 0.5–7 keV emission (blue) tends to fill in the cavities and voids in the mid-IR nebula. Regions where the diffuse X-rays are especially faint, notably a broad region bordering the ESE half of 30 Dor (Figure 3), tend to be filled in by MIR cloud structures (Figure 4), indicating that the cold clouds are located in front of the hot plasma in these locations and absorb the soft X-rays. In other regions, diffuse X-rays appear to surround or pass in front of bright MIR filaments (many examples are evident in Figure 5, especially panels c and d), revealing interfaces between the hot and cold ISM.

¹⁵ Our T-ReX diffuse map, combined with *JWST* images of the central portions of 30 Dor, was released publicly by the *Chandra* X-Ray Center in 2022 October, see <https://chandra.si.edu/photo/2023/30dor/index.html>.

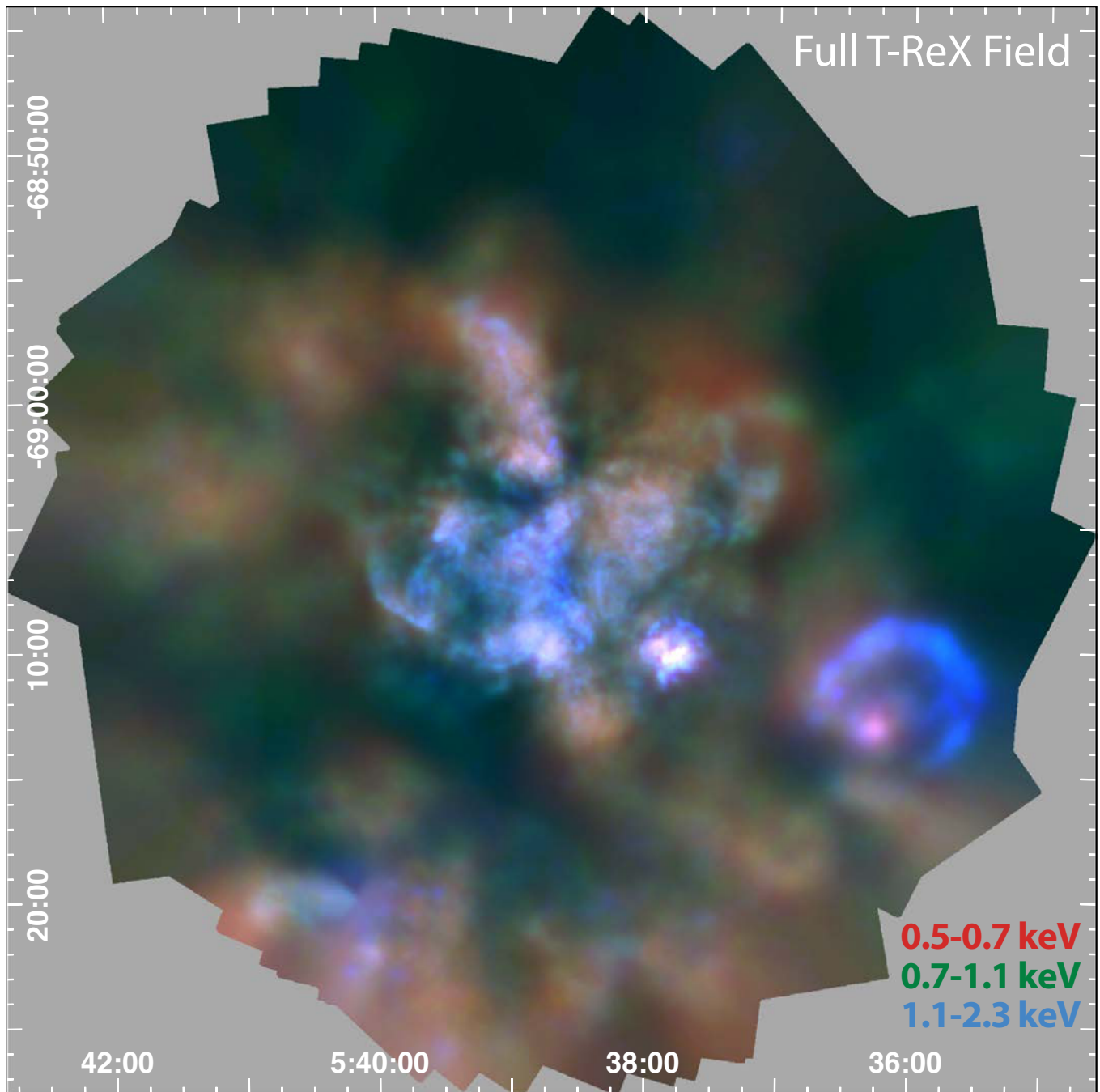


Figure 3. T-REX diffuse emission in three soft X-ray bands, smoothed with adaptive kernels to achieve $\text{SNR} = 15$. All 3615 point sources (seen in Figure 2 above) were excised before smoothing. Axes are in celestial (J2000) coordinates.

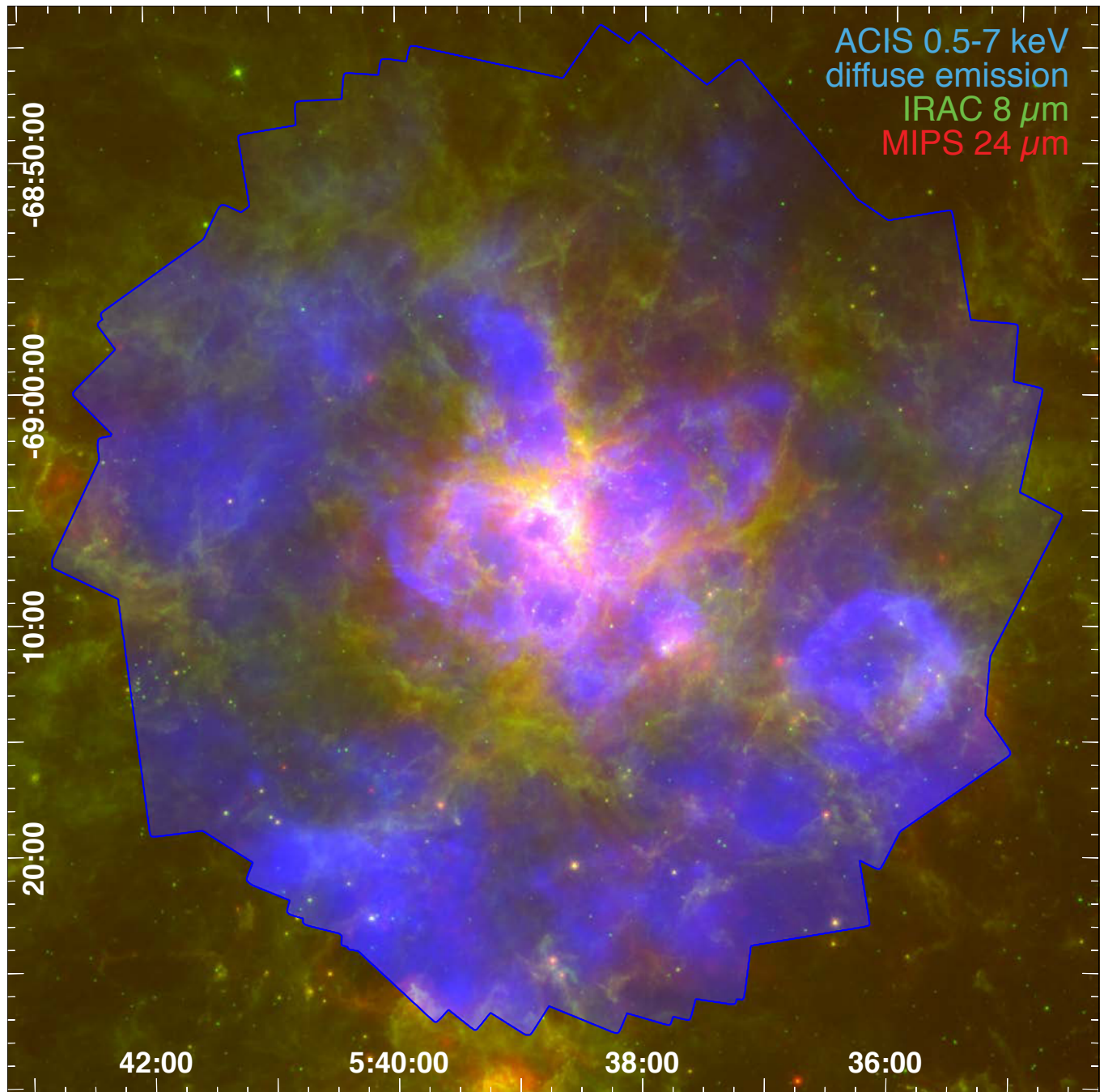


Figure 4. T-ReX diffuse emission in the *Spitzer* context. *Spitzer* images are from the Surveying the Agents of Galaxy Evolution (SAGE) survey (Meixner et al. 2006).

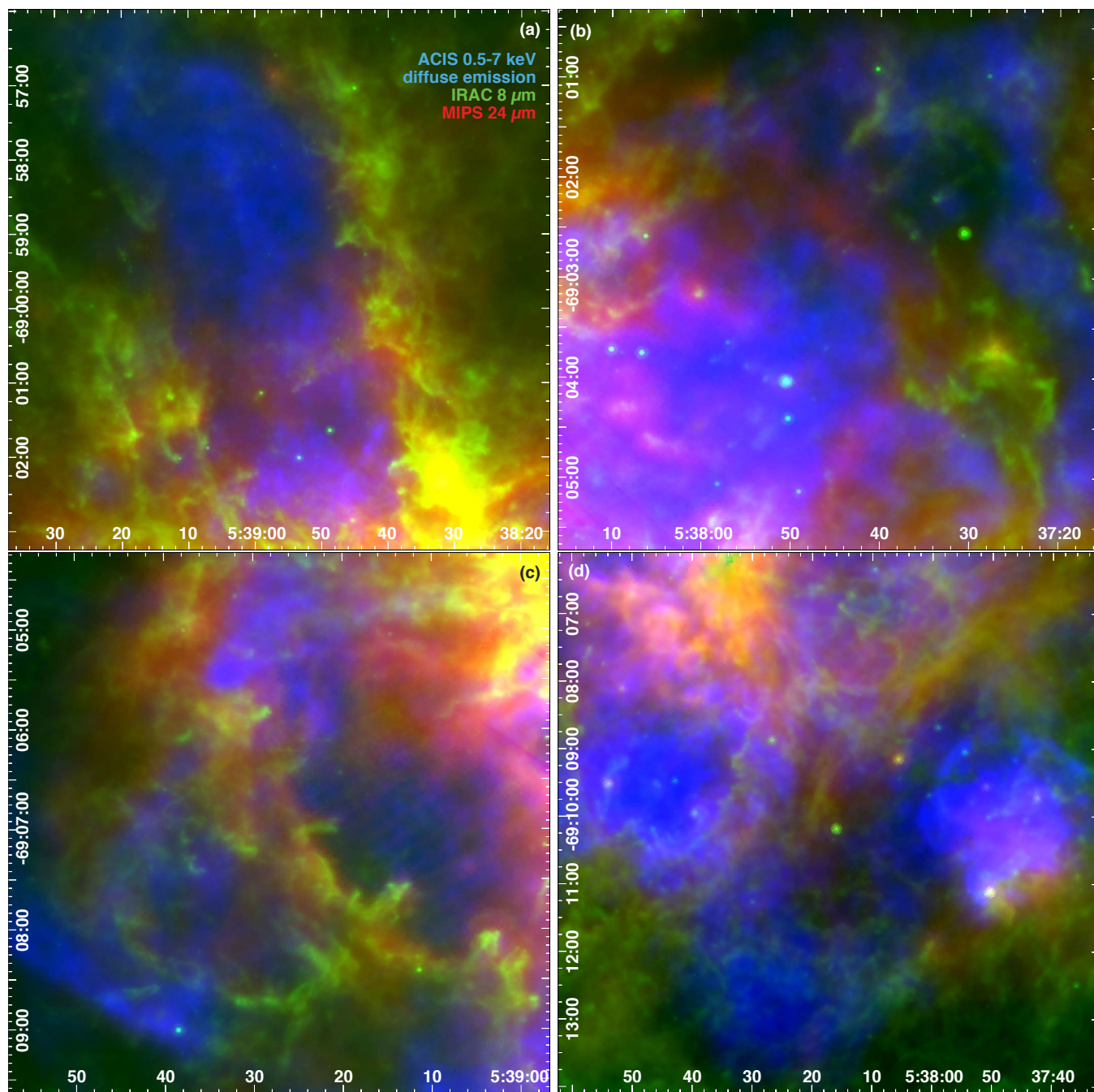


Figure 5. Light and shadow: zoomed and rescaled regions from Figure 4. These images illustrate the complex interfaces between the hot and cold ISM of 30 Dor. With respect to R136, these regions are located: (a) northeast; (b) northwest; (c) southeast; (d) southwest.

4. POINT SOURCES

In this and the following section we focus on the central region of the T-ReX field containing 30 Dor itself, imaged by the ACIS I-array (Figure 6). Point sources in the T-ReX catalog are distributed widely throughout this field, except in the vicinity of N157B, where bright diffuse emission prevented detection of point sources associated with NGC 2060 other than the extraordinarily bright, piled source PSR J0537–69 (source p1_255 with 3.4×10^5 net counts). The field center contains the R136 cluster, and we zoom in on this region in Figure 7 to better display its dense concentration of X-ray events and cluster of detected point-sources. The spatial distribution of regular sources exhibits more structure compared to occasional sources; besides R136 there are several smaller clusters of X-ray sources that appear to be associated with embedded subclusters (Walborn et al. 2013; Sabbi et al. 2016) in the molecular cloud to the north and west.

After the pulsar, most of the brightest point sources in the 30 Dor field are massive stars studied in detail by C22, including two Wolf-Rayet systems (Mk 34 and R140a) and the candidate high mass X-ray binary VFTS 399 (Clark et al. 2015). We present the cross-matching of T-ReX point sources with massive stellar counterpart catalogs in Appendix A; these matching lists, including blended sources in R136 (Figure 7) that could represent multiple OB stars, were used to construct the C22 sample. C22 found that the majority of Wolf-Rayet and Of/WN systems in 30 Dor were detected in X-rays (70.0% and 85.7%, respectively), but for O-type stars in general a similar majority went undetected, and the fraction of detected B-type stars was very low. The absorption-corrected X-ray luminosity (L_X) from spectral fitting of detected massive stars and upper limits on undetected massive stars indicate that the T-ReX massive star sample is highly incomplete for $\log L_X < 32$ ergs $^{-1}$.

We can also estimate the sensitivity of T-ReX to lower-mass, pre-main sequence stars. Among the regular sources in the T-ReX catalog, 1501/1871 (80%) were detected with >12 net counts. Assuming a typical T-Tauri X-ray spectrum and absorption equivalent to $A_V = 0.5$ mag, 12 counts on-axis corresponds to $\log L_X > 31.5$ ergs $^{-1}$. A calculation using the absorption-corrected surface brightness of the global diffuse emission (see Section 5 below) yields a very similar luminosity for a circular region of diffuse background emission enclosed by an on-axis point-source extraction aperture. Diffuse X-ray emission limits point-source sensitivity throughout the T-ReX field, not only in the brightest regions. This luminosity threshold suggests that T Tauri stars detected in T-ReX are likely to be in a mega-flaring state (Getman & Feigelson 2021). The *Chandra* Carina Complex Project (CCCP, Townsley et al. 2011a) provides a useful comparison to put this source luminosity in context, as it is a Galactic starburst region containing multiple stellar clusters with different ages, similar to 30 Dor (Cignoni et al. 2015; Povich et al. 2019). Nuñez et al. (2021) performed X-ray spectral fitting on 370 bright CCCP stellar sources that were not associated with OB stars. Imposing the T-ReX luminosity cut on the CCCP sample would exclude all but a small number ($\lesssim 20$) of flaring, low-mass T Tauri stars ($M < 2 M_\odot$). About one-third of intermediate-mass, pre-main sequence stars (IMPS; 2–4 M_\odot) in CCCP would be detectable in T-ReX, but with the caveat that their X-ray luminosity fades rapidly after ~ 1 Myr (Gregory et al. 2016; Nuñez et al. 2021). X-ray activity for pre-main sequence stars of all masses decays after ~ 7 Myr (Getman et al. 2022).

Considering the above arguments, T-ReX is sensitive primarily to early O stars and convective (flaring) IMPS, tracing the youngest stellar populations in 30 Dor, primarily R136. This explains why the older cluster Hodge 301 (20 Myr; Sabbi et al. 2016) is not detected in T-ReX. The great density of R136 itself means that the cluster core is not resolvable by ACIS, and (probably hundreds)

of unresolved stellar sources contribute to elevated diffuse X-ray backgrounds that further reduce point-source sensitivity in the vicinity (Figure 7). R136 contains the majority of stellar sources that should be detectable in principle, based on X-ray luminosity, but in reality this cluster also exhibits extreme source crowding and elevated diffuse background levels that dramatically reduced point-source sensitivity compared to the T-ReX field overall.

Beyond R136 and the neighboring smaller, embedded clusters, the point source population in the wider T-ReX field appears broadly consistent with a population of AGN and other background extragalactic sources, as indicated by the general lack of spatial clustering and the dearth of multiwavelength counterparts to T-ReX sources (see Appendix A). Using the 95% completeness limits of the 2-Ms *Chandra* Deep Field North catalog (CDF-N Alexander et al. 2003; Kim et al. 2004)¹⁶ as a control for the T-ReX field if the LMC were removed, we would predict 720 sources with soft-band (0.5–2 keV) flux $>8 \times 10^{-17}$ erg s⁻¹ cm⁻² and 480 sources with hard-band (2–8 keV) flux $>4 \times 10^{-16}$ erg s⁻¹ cm⁻². Assuming an average absorbing column through 30 Dor of $N_H = 2 \times 10^{22}$ cm⁻² and a characteristic photon index of 1.7, PIMMS¹⁷ shows that the limiting observed fluxes would be reduced to $\sim 1.2 \times 10^{-17}$ erg s⁻¹ cm⁻² in the soft band. The T-ReX catalog contains ~ 1600 regular sources above this soft-band limit, more than double the expected background contamination rate. By contrast, T-ReX contains only 525 hard-band sources brighter than the CDF-N 95% completeness limit (with absorption producing a negligible correction), hence the large majority of T-ReX sources detected in the hard band are consistent with background contaminants.

¹⁶ The CDF-S 2 Ms catalog (Luo et al. 2008) would yield very similar numbers.

¹⁷ <https://cxc.harvard.edu/toolkit/pimms.jsp>

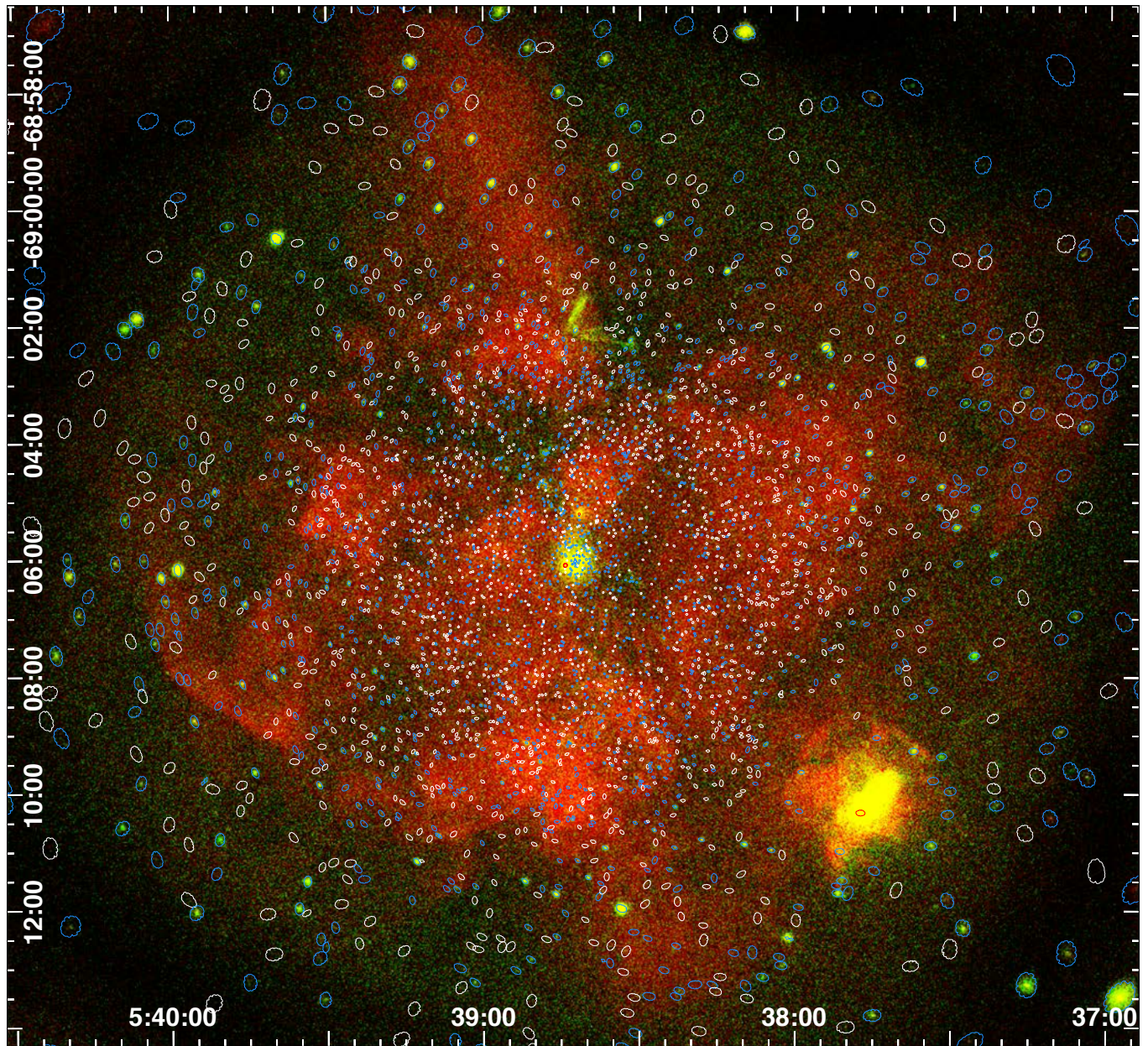


Figure 6. The T-ReX event data with point source extraction apertures overlaid, as in Figure 2, now zooming in on 30 Dor itself. Events are binned by 2 sky pixels.

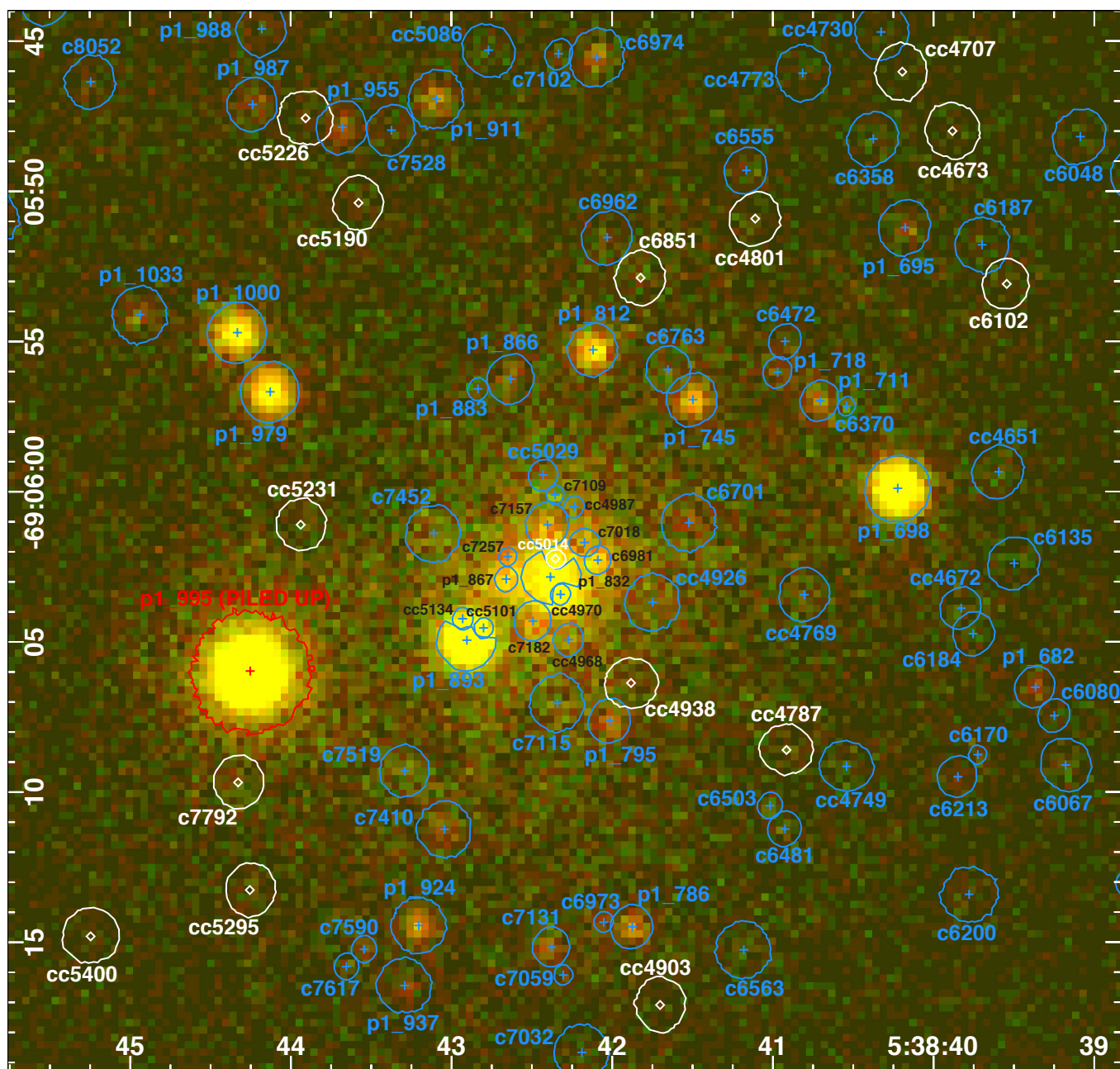


Figure 7. T-REX event data (as in Figures 2 and 6) zoomed in to show the inner $\sim 35'' = 8.4$ pc of the field, centered on the T-REX aimpoint (R136). Events are binned by 0.5 sky pixels. Source positions are shown as blue diamonds for occasional sources and as white crosses for regular sources, with their ACIS source labels (Table 2; regular source labels in the most crowded central region are shown in black, with reduced size, for clarity). The piled-up WR star Mk34 (p1_995) is noted in red.

5. DIFFUSE X-RAY EMISSION

30 Dor offers us a microscope on starburst astrophysics, having endured 25 Myr of the birth and death of the most massive stars known. Across its 250-pc extent, stellar winds and supernovae have carved the ISM within 30 Dor into an amazing display of arcs, pillars, and bubbles (Figures 4 and 5). For over 40 years, we have also known that 30 Dor is a bright X-ray emitter, so its familiar stars and cold ISM structures suffer irradiation by multi-million-degree plasmas. Here we focus on the diffuse X-ray emission revealed by T-ReX, highlighting hot/cold interfaces (Figure 5) and other hot plasma structures resolved to 1–10 pc scales across the entire 30 Dor complex (Figures 3 and 8). Massive star winds and cavity supernovae over the millenia have contributed to a broad mix of X-ray-emitting plasmas and absorbing columns, and the hot ISM within 30 Dor exhibits similar complexity as seen at colder temperatures. In Figure 8 we present a square approximately the size of the ACIS I-array ($17' = 245$ pc on a side), where the sensitivity and spatial resolution are maximized. In this section we present spectral fitting of the diffuse emission using extraction regions from within this image.

Townsley et al. (2011b,c) provided a detailed description of our general spectral modeling strategy as applied to the Carina Nebula, other Galactic massive star-forming complexes, and the 30 Dor observations predating T-ReX. The spectral model consists of 3 *vpshock* components; high timescales (e.g. $\log(\tau) = 13.7/[s \text{ cm}^{-3}]$) imply collisional ionization equilibrium (CIE) while lower timescales suggest the presence of non-equilibrium ionization (NEI) plasma. Each spectral fit plot presented below (Figures 9–11) labels the *vpshock* parameters for the various employed components: absorbing column (NH[123]), plasma temperature (kT[123]), timescale (τ [123]) and absorption-corrected surface brightness (SB[123]).

Abundances for most elements in the *vpshock* models were frozen at $0.4Z_{\odot}$, appropriate for the low-metallicity environment of the LMC (Russell & Dopita 1990), but we found that enhanced abundances of Ne ($0.59Z_{\odot}$), Mg $1.06Z_{\odot}$, and Si ($0.75Z_{\odot}$) were needed to account for other line features in the spectrum. Absorbing columns are modeled as *TBabs*; the values shown may be doubled to correct for LMC abundances.

Dotted Gaussians representing unmodeled lines were added because they substantially improve the fit (Townsley et al. 2011b,c). The central line energies, widths, and normalizations were all free parameters, and yet, as we demonstrate below, the multiple Gaussian components typically land on or near the energies of real X-ray emission lines. They may represent charge exchange (CX, see Gu & Shah 2023, for a recent review) or some other physics not captured by the current plasma models.

We also allow a contribution from unresolved pre-MS stars (2-temperature *apec* model) and an absorbed power law to account for a hard tail in the spectrum due to a background of unresolved AGN and/or nonthermal emission in 30 Dor.

5.1. N157B SNR and Pulsar Wind Nebula

The N157B SNR (also known as 30 Dor B) and the associated wind nebula produced by its pulsar, PSR J0537 (Marshall et al. 1998; Wang et al. 2001), produce the brightest diffuse X-ray emission by far in the T-ReX field, with (absorption-corrected) surface brightnesses exceeding the typical values of 30 Dor itself by one to two orders of magnitude. It was therefore critical to remove these diffuse sources prior to modeling the global diffuse emission of 30 Dor.

We present spectral fits to N157B and the pulsar wind nebula in Figure 9. N157B required a complex model consisting of three thermal plasma components plus a power law of comparable

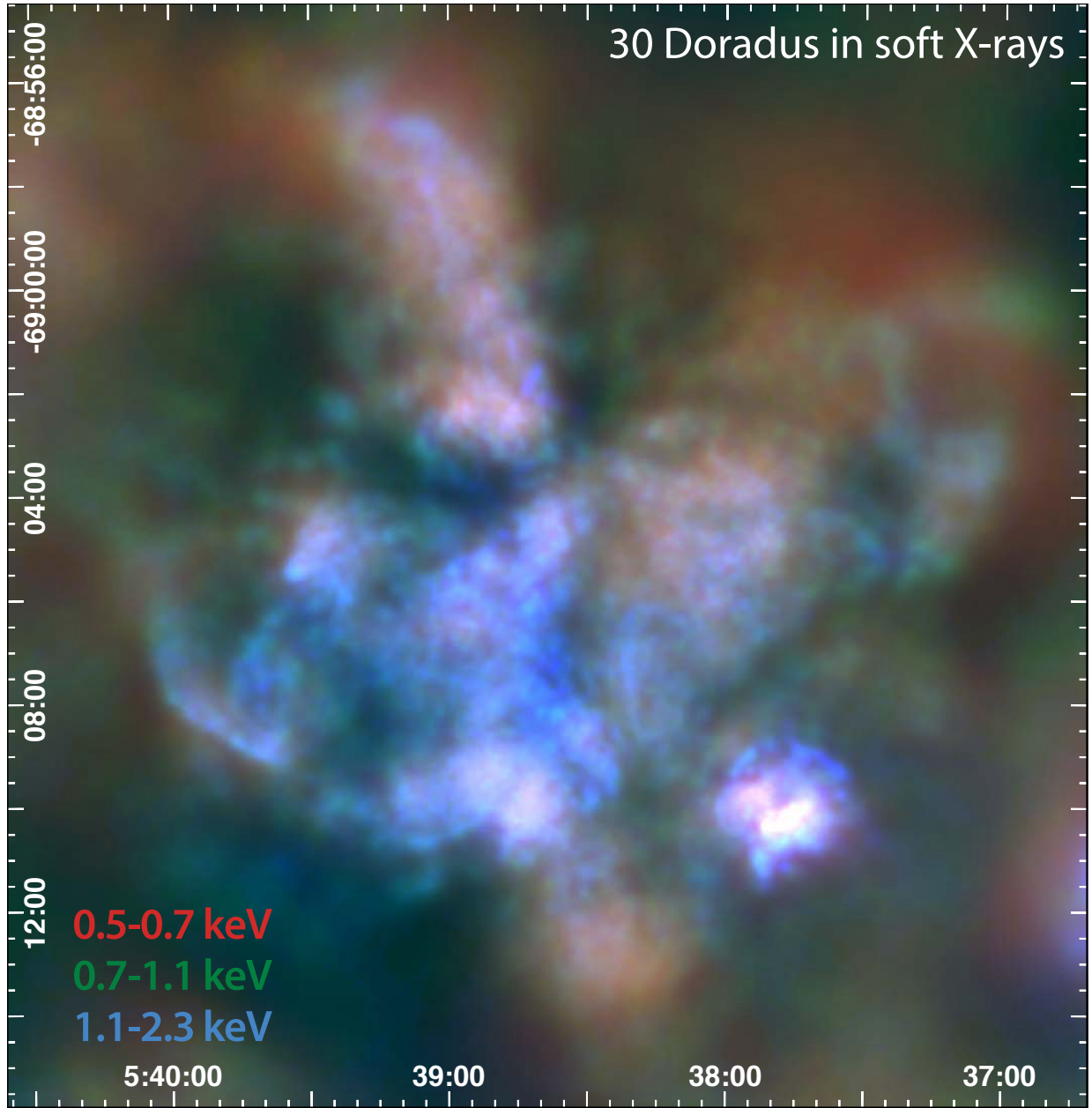


Figure 8. 30 Dor diffuse emission in three soft X-ray bands. This is a zoom of Figure 3, cropped to a similar field as shown in Figure 6.

brightness. The two thermal plasma components used to model the soft end of the diffuse spectrum have $kT_1 \approx kT_2 = 0.25$ keV, and [Chen et al. \(2023\)](#) recently concluded that the combination of the soft X-ray plasma and the physical extent of N157B require at least one more supernova preceded the one, 5000 years ago, that created PSR J0537.

Our model also includes 10 Gaussian line components, many of which correspond to energies of emission lines that show CX enhancement in the Cygnus Loop SNR ([Katsuda et al. 2011](#); [Uchida et al. 2019](#)) or starburst galaxies ([Ranalli et al. 2008](#); [Liu et al. 2012](#); [Zhang et al. 2022](#)). The O VII triplet falls near 0.53 keV, while O VIII can produce lines near 0.61 keV and 0.75 keV. Highly-ionized iron can produce the lines near 0.88 keV (Fe XVII or Fe XVIII) and 0.94 keV (Fe XIX), but the latter

could also be Ne IX. Other ionized neon and/or magnesium lines could produce the components at 1.07 keV (Ne X), 1.17 keV (Ne X or Mg), 1.35 keV (Mg XI), and 1.60 keV (possibly Mg).

The two components attributable to magnesium CX lines also appear in the modeled spectrum of the pulsar wind nebula, which otherwise presents a comparatively simple, power-law spectrum requiring only one additional NEI plasma component to model the soft tail of the spectrum. This model resembles that of the combined ACIS-S spectrum of N157B and the pulsar wind nebula presented by [Chen et al. \(2006\)](#).

Unique among the T-ReX diffuse spectra modeled thus far, the fit to the hard tail of the N157B was significantly improved by the addition of a Gaussian component at 6.38 keV corresponding to the Fe $K\alpha$ fluorescence line. This is a common feature in AGN and some X-ray binaries, arising in dense accretion disks at high temperature. It is unlikely that this emission arises in the low-density SNR, but it could be produced by massive, colliding-wind binaries present in the massive NGC 2060 stellar cluster that hosted the supernova progenitor (see, e.g., [Walborn et al. 2014](#)). This line is obvious in the X-ray spectrum of the η Car system, for example ([Kashi et al. 2021](#)). The average X-ray luminosity of the strongly variable η Car is 6.33×10^{34} erg s $^{-1}$, which would rank it among the brightest T-ReX point sources but still an order of magnitude fainter than PSR J0537-69, the sole point source detected in the central regions of N157B.

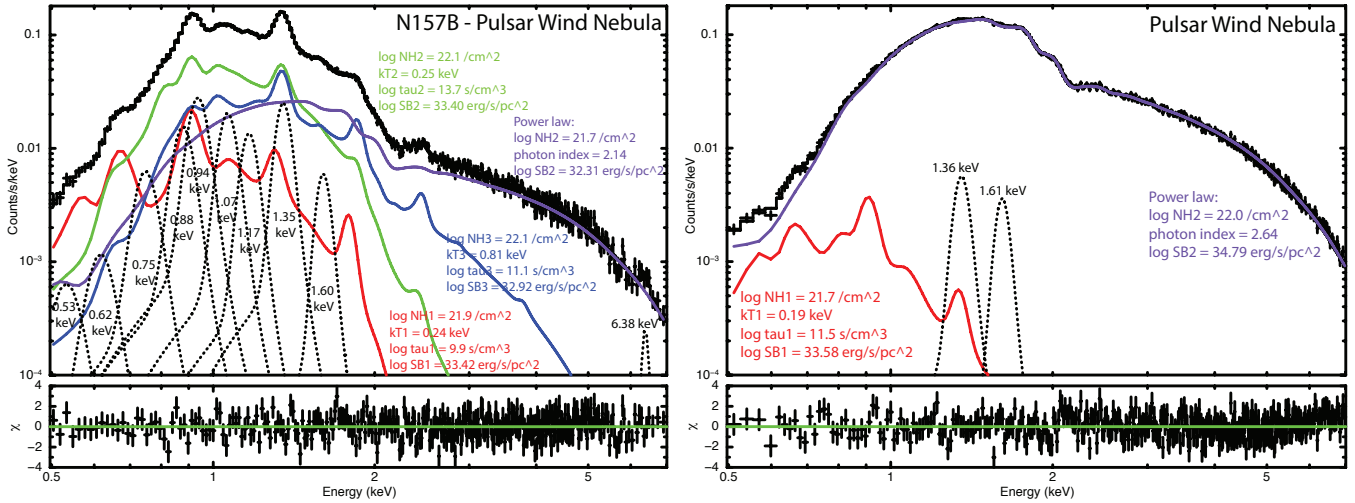


Figure 9. Diffuse X-ray spectra of N157B. (a) The N157B SNR spectrum with the central PWN removed. (b) The J0537 PWN spectrum with the PSR J0537 point source removed. In these and other plots of spectral fitting presented below, the following parameters of various numbered models components are labeled: N_H (absorbing hydrogen column density), kT (plasma temperature), tau (timescale), and SB (surface brightness, corrected for absorption NH).

5.2. Spectral Fits to Global Diffuse Emission

The spectrum “Global – N157B” presented in [Figure 10](#) includes everything inside the outer tessellate boundary (red outline with the approximate shape of the state of Texas) shown in [Figure 11](#), but excluding the very bright N157B supernova remnant and its pulsar wind nebula (see the previous subsection). The global boundary was chosen based on a constant level of soft-band, smoothed photon

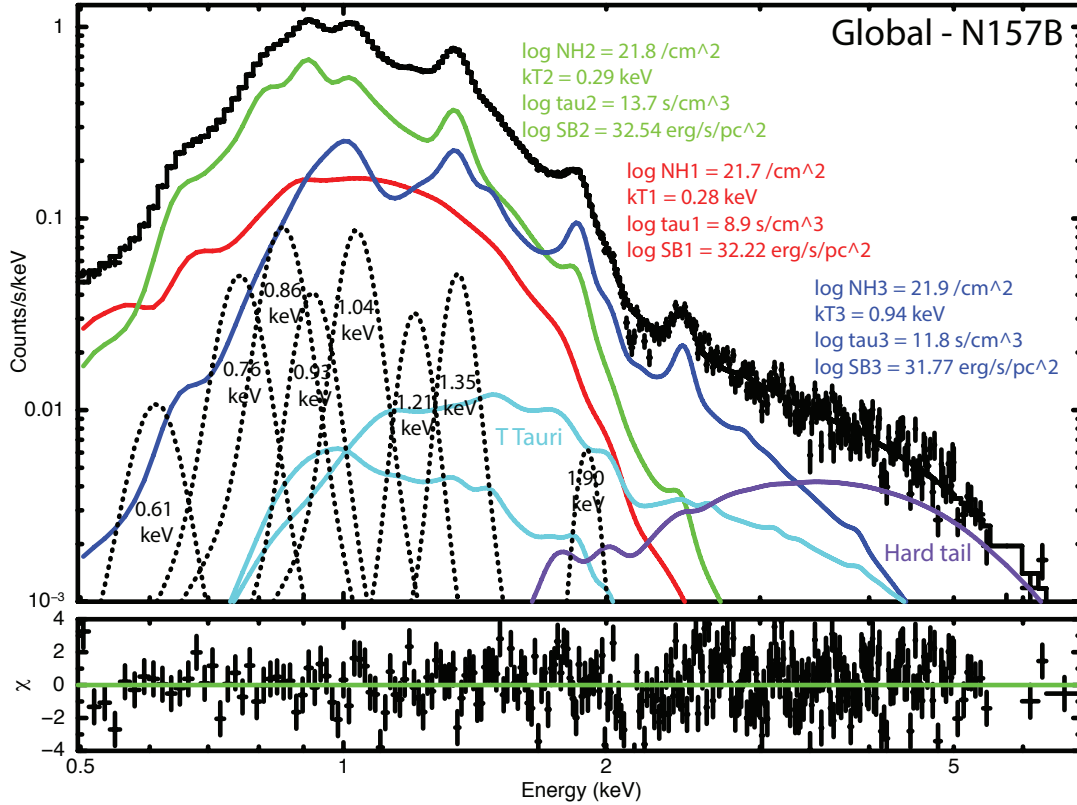


Figure 10. The global diffuse X-ray spectrum of 30 Dor, with the N157B SNR and its PWN removed. The “Global” diffuse region is defined in Figure 11 below.

flux that enclosed the brightest diffuse emission associated with 30 Dor. This integrated diffuse X-ray emission spectrum has 1.7×10^6 net counts.

The 8 brightest T-ReX point sources (those with $\text{NetCounts}_{\text{t}} > 10^4$ in Table 2) total 2.55×10^6 X-ray counts, however most of this contribution comes from outside the area enclosed by the global boundary, in the off-axis regions and PSR J0537. The fainter point sources in the 30 Dor field provide an order of magnitude fewer aggregate net counts, 2.2×10^5 , or 13% of the global diffuse counts.¹⁸ The spectral model component representing unresolved T Tauri stars represents <1% of the diffuse emission (Figure 10).

The fits to the global spectrum in Figure 10 included 8 Gaussians with energies between 0.5 and 2 keV, some of which could plausibly represent CX-enhanced line emission and several of which were also used in the fit to the spectrum of N157B (see Figure 9). Absent from the global spectrum are Gaussian components at the energies of the magnesium lines, seen in both the SNR and pulsar wind nebula spectrum. One new Gaussian component appears at 1.90 keV and could represent the Si XIII emission observed in starburst galaxies (Ranalli et al. 2008; Katsuda et al. 2011).

¹⁸ T-ReX has enabled a significant improvement in faint point-source extraction compared to our early analysis of the first, shallow observations of 30 Dor, for which extracted point sources represented 9% of the integrated diffuse emission (Townsend et al. 2006a,b).

5.3. Sample Tessellate Spectral Fits

Employing the strategy developed for CCCP (Townesley et al. 2011b), we subdivided the 30 Dor diffuse emission into tessellates using the *WVT binning* algorithm (Diehl & Statler 2006). This method allows for higher spatial resolution in regions of brighter emission while maintaining a constant SNR across all extracted spectra. Using SNR=70, we needed 308 tessellates to tile the field enclosed by the “Global” contour (Figure 11). The starting point for spectral fits to each extracted tessellate spectrum was the global model with no Gaussian components. Unneeded components were then removed, fits optimized, and Gaussians added last if they improved the fit.

Many tessellates (e.g. 188, and, with the addition of Gaussian lines, 305, 293, 92, 21, and SE Ridge) can be modeled with just *vpshock2*, a soft CIE plasma that usually dominates the surface brightness, and *vpshock3*, a harder plasma that may be NEI or CIE. Of course the absorptions, temperatures, and timescales of these plasmas vary across the complex, creating 30 Dor’s rich X-ray appearance.

The soft *vpshock1* component usually has the same temperature as *vpshock2* but a much shorter ionization timescale, implying an NEI plasma. Thus tessellates requiring *vpshock1* may indicate the presence of a plasma transitioning from NEI to CIE. This component is needed only in tessellates 189 and 239, which have the lowest apparent surface brightnesses of all sample tessellates due to high absorption north of R136. Tessellate 189 additionally required the brightest unresolved TTS components among the sample tessellates, representing the embedded stellar population north of R136 (Sabbi et al. 2016).

Tessellate 131 provides a sample of the diffuse plasma nearest to R136. Unsurprisingly, it includes relatively strong components modeling the unresolved T Tauri population. The absorption to all components is higher than the Global average, and the diffuse spectrum here is significantly harder, requiring both a CIE thermal plasma with $kT3 = 1.3$ keV and an hard tail. Tessellates 21 and 189, the other two samples of the central regions of 30 Dor (Figure 11), have hot thermal plasma components with the same temperature but shorter timescales, implying NEI.

Comet and SE Ridge are names given to two hand-drawn tessellate boundaries encircling areas of unusually bright, apparently hard diffuse emission. Comet was the only sample tessellate fit with single CIE plasma component, while SE Ridge required two CIE plasmas and several Gaussian lines. The hotter $kT3 = 0.69$ keV component dominates SE Ridge more than in most other regions. Both tessellates show higher absorption than the Global average, suggesting regions where hot plasma encounters cold gas at the western edge of the 30 Dor superbubble.

If Comet and SE Ridge represent regions of plasma confinement and possible mixing with the cold ISM, sample tessellates 305 and 92 appear to sample regions at the northern and southern extremes, respectively, where there could be champagne flows of diffuse plasma leaking from 30 Dor. The X-ray flux appears softer in these lobes (Figures 8 and 11), and indeed the absorption is lower here compared to central regions and to the Global average. Figures 5a and b show that the X-ray plasma in these regions fills cavities outlined by PAH emission.

5.4. The Manta Ray: A New Candidate Pulsar Wind Nebula

The Manta Ray (named for its morphological resemblance to the large, flat-bodied, winged fish that “flies” under the sea) is an unusually hard, extended X-ray source located 4’ north of R136. This feature is visible as a green “V” shape in the event data displayed in Figure 6. It required a custom, hand-drawn aperture to extract its diffuse emission. We fit the spectrum of the Manta Ray

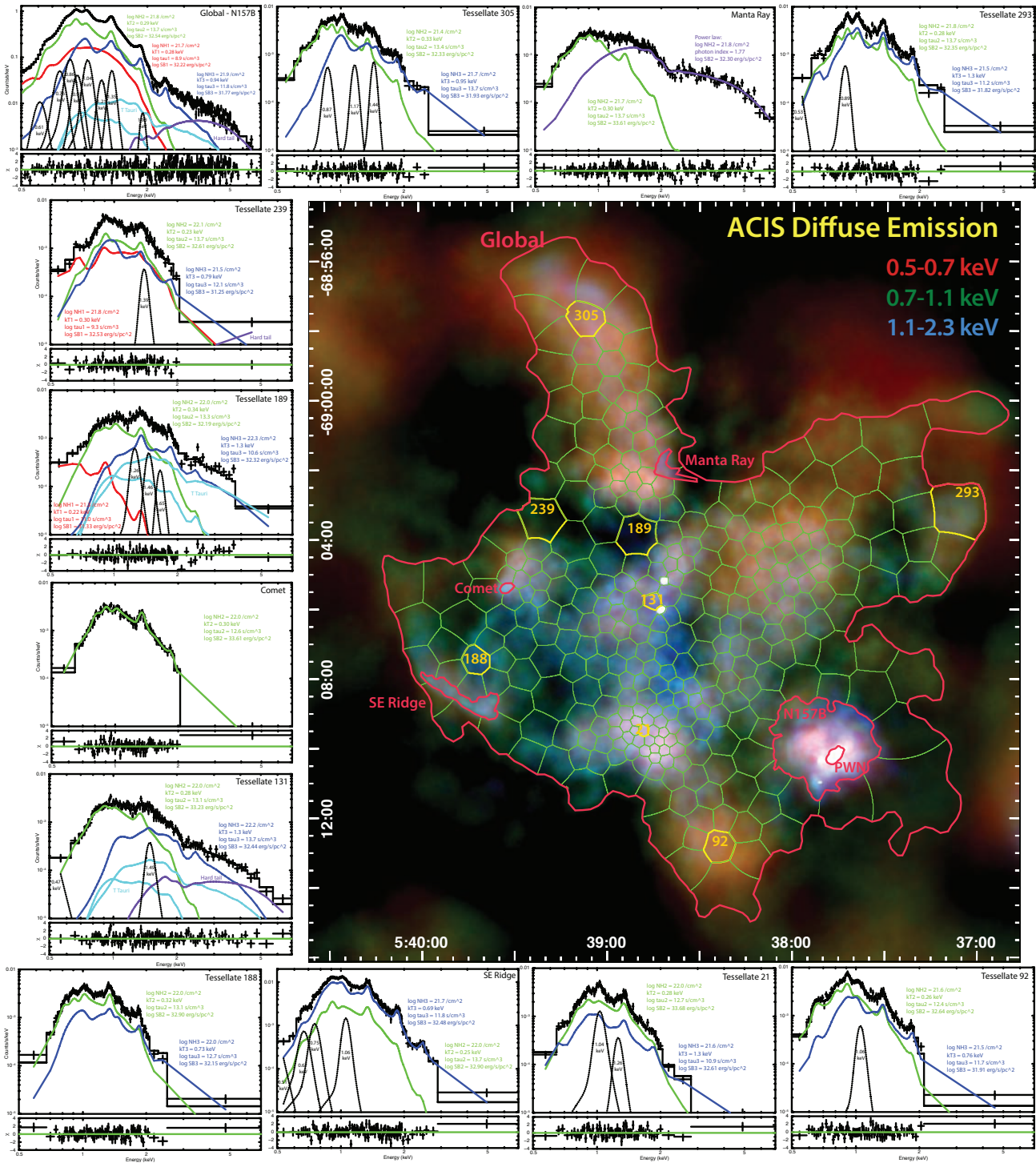


Figure 11. Tesselation used for spatially-resolved spectral fitting analysis of the ACIS diffuse emission. Spectral fits to 11 sample extractions representing a range of locations and regions of interest (labeled in red and yellow in the soft diffuse image) illustrate the spectral complexity and diversity of the diffuse X-ray emission in 30 Dor. The outer boundary defines the “global” diffuse spectrum (Figure 10), plotted in the upper-left panel to facilitate comparison with the smaller extraction regions. Global and the other named regions outlined in red are based on surface brightness contours: N157B and PWN (Figure 9), Manta Ray, Comet, and SE Ridge. The 308 tessellates (in green and yellow) come from the *WVT Binning* code by Diehl & Statler (2006).

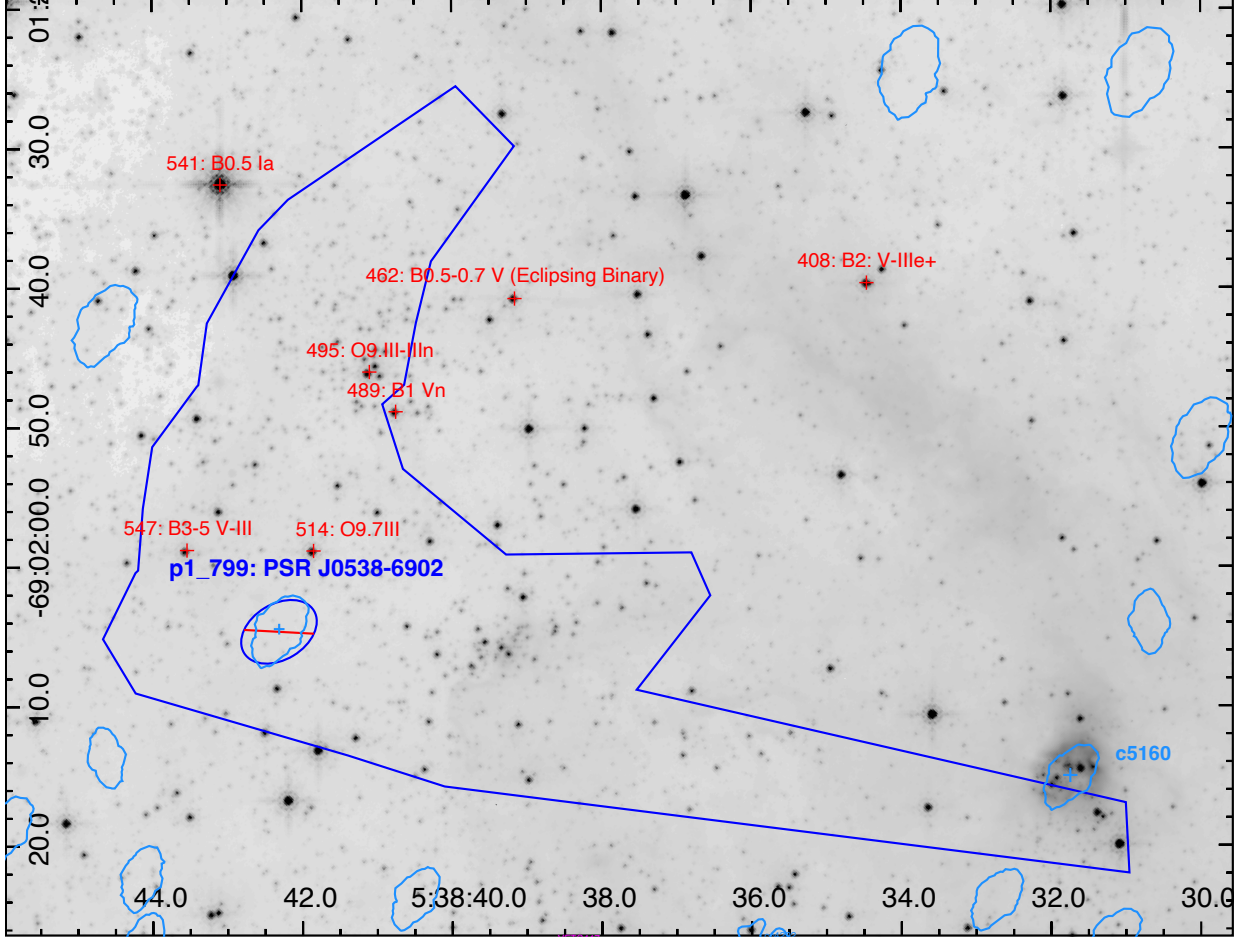


Figure 12. HTTP F160W image (Sabbi et al. 2013) showing the stellar content in the region of the Manta Ray diffuse extraction tessellate (blue outline). Three stellar overdensities are visible along the trailing edges of the Manta Ray “wings;” the one at lower-right also shows NIR nebulosity suggesting an embedded cluster associated with the T-ReX point source c5160. The candidate X-ray pulsar (PSR J0538-6902 = T-ReX catalog source p1_799) is marked with a blue + sign enclosed by red-blue ellipse showing mask used to exclude the source from the diffuse emission. OB stars from VFTS (Walborn et al. 2014; Evans et al. 2015) are marked with red + symbols with spectral types labeled; the majority are evolved massive stars. Extraction apertures for regular T-ReX catalog sources are outlined with blue polygons (occasional sources are omitted).

using a similar model as with N157B and its PWN (see Figure 9) and found that it needed only two components (Figure 11). The soft portion of the spectrum was fit with a CIE plasma with $kT = 0.30$, $\log N_H/\text{cm}^{-2} = 21.7$, and $\log \text{SB}/(\text{erg s}^{-1} \text{pc}^{-2}) = 33.61$. The hard spectrum required a power-law with $\alpha_{\text{PWN}} = 1.77$, $\log N_H/\text{cm}^{-2} = 21.8$, and $\log \text{SB}/(\text{erg s}^{-1} \text{pc}^{-2}) = 32.30$.

We used a power-law with LMC absorption ($TBvarabs*pow$) to fit the spectrum of the T-ReX point source p1_799 (585 net counts), which is located near the center of the Manta Ray but has no apparent counterpart at visible/NIR wavelengths (Figure 12). The spectral fits returned $N_H = 2.71^{+1.1}_{-0.9} \times 10^{22} \text{ cm}^{-2}$ (for $Z = 0.4$), power-law index $\alpha_{\text{PSR}} = 1.5 \pm 0.3$, and $\log L_{t,c} = 33.42$ (0.5–8 keV total-band luminosity). Comparing the power-law indices of the Manta Ray diffuse emission (α_{PWN})

with its point source (α_{PSR}) reveals very good agreement with the empirical relationship between the spectra of young X-ray pulsars and their wind nebulae derived by [Gotthelf \(2003\)](#). These α values imply a spin-down luminosity of $L_{\text{sd}} \sim 0.8\text{--}1.5 \times 10^{37}$ erg s $^{-1}$ for the driving pulsar. Based on the broad correlation between L_X and L_{SD} reported by [Possenti et al. \(2002, their Fig. 2\)](#), we would expect $L_X \sim 5 \times 10^{33}$ erg s $^{-1}$ for the pulsar, in very good agreement with the absorption-corrected $L_{t,c}$ for p1_799. We therefore propose that p1_799 be designated PSR J0538-6902, the candidate pulsar responsible for generating the Manta Ray PWN.

Additional lines of circumstantial evidence also support the conclusion that the Manta Ray is a PWN. Since the diffuse absorption was modeled assuming solar metallicity using *TBabs*, doubling its value yields $N_H = 1.26 \times 10^{22}$ cm $^{-2}$ for the power-law nebular component at LMC metallicity, which is similar to the absorption of the point source PSR J0538-6902. There are several evolved, massive stars and three compact star clusters in the vicinity of the Manta Ray ([Figure 12](#)), which could trace a massive stellar association that hosted the progenitor of the pulsar. The arc-shaped morphology of the PWN suggests a bow shock resulting from a high space velocity for the pulsar in an easterly direction. Assuming, for example, that the progenitor resided in the nearest HTTP cluster ($\sim 15'' = 3.6$ pc away), and also assuming a typical neutron star birth velocity of ~ 200 km/s ([Sartore et al. 2010](#)), PSR J0538-6902 could have reached its present-day location $\sim 20,000$ yr post-supernova. An age of a few $\times 10^4$ would be consistent with the X-ray luminosity of PSR J0538-6902 ([Possenti et al. 2002](#)), making it ~ 10 times older and hence ~ 1000 times less luminous than PSR J0537-6910 in N157B ([Chen et al. 2006](#)).

5.5. Physical Properties of the Global Diffuse X-ray Emission in 30 Dor

To estimate the physical conditions of the diffuse X-ray plasma within 30 Dor, we follow the approach used in previous work for M17 ([Townesley et al. 2003](#)) and the Carina ([Townesley et al. 2011b](#)) to produce [Table 3](#). These three massive star-forming complexes span more than an order of magnitude in bolometric luminosity and physical size. Both 30 Dor and Carina clearly host multiple generations of massive star formation over the past ~ 10 Myr ([Povich et al. 2019; Cignoni et al. 2015](#)). M17 is the least luminous and most compact of the three, with the youngest rich cluster, the 0.5-Myr-old NGC 6618—but here, too there is evidence for a more evolved and spatially distributed massive stellar population ([Povich et al. 2009; Getman et al. 2014](#)).

Compared to previous work on much shallower *Chandra* observations, our Global model now includes a softer (0.28 keV) NEI component in 30 Dor, similar to both M17 and Carina ([Townesley et al. 2011c](#)). The hardest, *kT3* component is hotter in 30 Dor (0.94 keV) than in M17 or Carina (both 0.6 keV). Both 30 Dor and Carina have similar X-ray plasma densities ($n_{e,x} \sim 10^{-2}$ cm $^{-3}$) and pressures ($P_x/k \sim 10^5$ K cm $^{-3}$), while the corresponding densities and pressures in M17 are higher by an order of magnitude. This difference seems to indicate that the hot plasma is more confined in M17 compared to the two larger, more evolved complexes.

The assumed volume (ηV_x) of the hot plasma region in 30 Dor is about 50 times greater than that of Carina, while the total-band, absorption-corrected luminosity ($L_{t,c}$) is ~ 120 times greater ([Townesley et al. 2011b](#)). Based on scaling the total energy and mass (E_x and M_x) of the hot plasma in Carina as $(L_{t,c}\eta V_x)^{1/2}$, we would expect these quantities to be roughly 10 times greater in 30 Dor, but instead we find they are 65–75 times greater.

Table 3. Physical Properties of the Diffuse Plasma Components

Parameter	Scale factor	T-ReX “Global” Region		
		vpshock1	vpshock2	vpshock3
Observed X-ray properties				
median kT_x (keV)	...	0.28	0.29	0.94
L_{tc} (erg s ⁻¹)	...	6.2×10^{36}	12.9×10^{36}	2.2×10^{36}
V_x (cm ³)	η	5.5×10^{61}	5.5×10^{61}	5.5×10^{61}
Derived X-ray plasma properties				
T_x (K)	...	3.2×10^6	3.4×10^6	10.9×10^6
$n_{e,x}$ (cm ⁻³)	$\eta^{-1/2}$	0.05	0.07	0.03
P_x/k (K cm ⁻³)	$\eta^{-1/2}$	3.4×10^5	5.1×10^5	6.8×10^5
E_x (erg)	$\eta^{1/2}$	3.9×10^{51}	5.8×10^{51}	7.7×10^{51}
τ_{cool} (Myr)	$\eta^{1/2}$	20	14	111
M_x (M _⊙)	$\eta^{1/2}$	1358	1964	809

NOTE—Equations detailing how the derived properties were obtained from the observed properties are given in [Townesley et al. \(2003\)](#). The volume is assumed to be the area of the “Global” diffuse region multiplied by a depth of 50 pc. The quantity η is a “filling factor,” $0 < \eta < 1$, accounting for partial filling of the “Global” volume with the X-ray-emitting plasmas. The parameters in the table should be multiplied by the appropriate scale factor (Column 2) to account for this filling factor. Derived plasma properties are proportional to $\eta^{1/2}$ and are thus only weakly sensitive to this correction.

We can also compare the luminosity of the diffuse X-ray emission to the combined bolometric luminosity of the massive stars in each region. For 30 Dor, $L_{bol} = 3 \times 10^{41}$ ([Lopez et al. 2011](#)) yields $\log L_{t,c}/L_{bol} = -4.15$. Adopting $L_{t,c}$ from [Townesley et al. \(2011c\)](#) and L_{bol} from ([Binder & Povich 2018](#)), we have $\log L_{t,c}/L_{bol} = -5.70$, -5.52 , and -6.04 for Carina, NGC 3603, and M17, respectively, in the Milky Way.

Based on the above simple comparisons, the superlative mass, energy, and luminosity of the X-ray-emitting plasma in 30 Dor require enhanced mass-loss and high-energy feedback for this starburst region, exceeding expectations for scaled-up versions of the Galactic regions.¹⁹ Multiple supernova explosions have likely contributed to the diffuse plasma. A SN shock propagating at $v_{shock} > 100$ km s⁻¹ (e.g., [Chen et al. 2023](#)) would cross the diameter of the T-ReX field in < 0.5 Myr, and we have already discussed the abundance of evidence for recent SNe in the form of pulsars (+wind nebulae such as the Manta Ray) associated with evolved massive clusters.

The brightest diffuse emission, however, is centered on R136, which is too young to have experienced SNe. This points to a wind origin, driven by the higher mass-loss rates of the numerous Wolf-Rayet and other supermassive stars in this extraordinarily rich cluster ([Nugis & Lamers 2000](#); [Vink & de](#)

¹⁹ While a smaller filling factor η for the 30 Dor plasma compared to the Galactic regions is plausible, its value would need to be vanishingly small to explain the differences in mass and energy in these comparisons, and η does not factor into the luminosity calculation at all.

Koter 2005, C22). Example tessellates in outer regions of 30 Dor that could plausibly be dominated by SN-driven bubbles (92, 293, and 305; see Figure 11) have 15%–25% the absorption-corrected surface brightness of tessellate 131, which samples diffuse plasma closest to R136, hence 70–85% of the diffuse X-ray luminosity in the central regions could be wind-generated.

6. LEGACY VALUE OF T-REX

In this overview of the T-ReX project, we have provided numerous data products, including a point-source catalog, diffuse emission images and spatially-resolved spectra (Section 2.7). The analysis presented in this work only scratches the surface of this unprecedentedly deep and rich X-ray dataset. T-ReX provides our best opportunity to dissect the high-energy emission from a starburst region. These galactic building blocks all emit X-rays, but they blur together in distant starburst galaxies. With T-ReX, we have quantified the relative contributions of the diverse sources that constitute the X-ray emission of a starburst. The stars themselves (single very massive stars, magnetic OB stars, colliding-wind binaries, and lower-mass pre-MS stars) and their stellar remnants (pulsars, X-ray binaries) are generally resolved and hence can be separated from truly diffuse shock emission (from massive stellar winds, individual young SNRs, thermalized cavity SNRs, and PWNe). T-ReX provides the largest number of diffuse X-ray emission counts ever detected from a massive star-forming region, surpassing Carina (Townesley et al. 2011c) and Cygnus OB2 (Albacete-Colombo et al. 2023).

A rich history of multiwavelength studies leverages 30 Dor as a bridge from Galactic to extragalactic studies. T-ReX emerges as a singularly powerful dataset for study of diffuse emission and feedback, but it has also revealed the limits of current X-ray instrumentation in studying resolved stellar populations beyond the Milky Way. While point sources become fainter with distance, X-ray surface brightness is a conserved quantity, and we have shown that the exceptionally bright diffuse emission in 30 Dor adversely affects the point-source sensitivity limits, which was not the case in Carina and other Galactic GHuR s (Townesley et al. 2011c). Even *Chandra's* unmatched spatial resolution is no match for the level of crowding and source confusion at the center of the R136 cluster (see also C22).

T-ReX will remain the best dataset available for the foreseeable future for the analysis of diffuse X-ray emission in active star-forming regions, including evidence for charge exchange processes at hot/cold ISM interfaces. Gratings spectroscopy with current instruments, while successfully applied to young Galactic supernova remnants and more distant starburst galaxies, cannot probe the lower surface brightness of plasmas generated by stellar winds and cavity supernovae. There is need for still better spatial resolution to resolve out contributions from bright point sources that outshine the diffuse emission in more distant galaxies. Further analysis of the T-ReX data should map the variations in X-ray absorption-corrected surface brightness, plasma temperature, density, pressure, and metallicity across 30 Dor, better quantifying the effects of feedback from massive stars on the evolution of star-forming regions and their host galaxies.

We thank Breanna Binder and Anna Rosen for helpful discussions, offering their perspectives as, respectively, an extragalactic high-energy observer and a theoretician of massive stellar feedback processes.

This work was supported by the *Chandra X-ray Observatory* Guest Observer grants GO5-6080X (PI: L. Townsley) and GO4-15131X (PI: L. Townsley) and by the Penn State ACIS Instrument Team Contract SV4-74018. Both of these were issued by the *Chandra X-ray Center*, which is operated by the Smithsonian Astrophysical Observatory for and on behalf of NASA under contract NAS8-03060. M. Povich acknowledges support from the National Science Foundation under award AST-2108349 (RUI). The ACIS Guaranteed Time Observations included here were selected by the ACIS Instrument Principal Investigator, Gordon P. Garmire, of the Huntingdon Institute for X-ray Astronomy, LLC, which is under contract to the Smithsonian Astrophysical Observatory; Contract SV2-82024.

This research used data products from the *Chandra Data Archive*, software provided by the *Chandra X-ray Center* in the application package *CIAO*, and the *SAOImage DS9* software developed by the Smithsonian Astrophysical Observatory.

This research also used data products from the *Spitzer Space Telescope*, operated by the Jet Propulsion Laboratory (California Institute of Technology) under a contract with NASA.

This work used data products from the NASA/ESA Hubble Space Telescope, obtained at the Space Telescope Science Institute, which is operated by AURA Inc., under NASA contract NAS 5-26555.

This work also used data from the ESA mission *Gaia* (<https://www.cosmos.esa.int/gaia>), processed by the *Gaia* Data Processing and Analysis Consortium (DPAC, <https://www.cosmos.esa.int/web/gaia/dpac/consortium>); funding for the DPAC has been provided by national institutions, in particular the institutions participating in the *Gaia* Multilateral Agreement.

This research has also made use of NASA’s Astrophysics Data System Bibliographic Services, and the SIMBAD and VizieR databases operated at the Centre de Données Astronomique de Strasbourg.

Facilities: CXO (ACIS), Gaia, ESO:VISTA (VIRCAM), VLT:Kueyen (FLAMES-ARGUS), HST (WFC3, ACS), Spitzer (IRAC, MIPS), WISE Herschel (SPIRE).

Software: *ACIS Extract* (Broos et al. 2010, 2012; Broos & Townsley 2016), *CIAO* (Fruscione et al. 2006), *DS9* (Joye & Mandel 2003), *MARX* (Davis et al. 2012) *XSPEC* (Arnaud 1996).

APPENDIX

A. POSSIBLE OPTICAL/IR COUNTERPARTS TO X-RAY POINT SOURCES

Identifying optical-infrared (OIR) counterparts to *Chandra* sources (“matching” X-ray and OIR catalogs) is often a challenging task. The dynamic range of flux sensitivity for any OIR catalog will typically be narrower than the apparent OIR fluxes of the objects detected by *Chandra*. For example, when the absorbing column and astrophysical classification of an X-ray source are unknown, its apparent magnitude could span a range $\gtrsim 15$ in J (Getman et al. 2011; Broos et al. 2013). The difference in spatial resolution of an OIR catalog compared to the $\sim 0.5''$ on-axis resolution of ACIS complicates the notion of a simple, one-to-one match, as in cases of large resolution departures (beyond a factor of 2) a single source in the lower-resolution catalog will frequently overlap with

multiple sources in the other. The population of X-ray sources without detected OIR counterparts can significantly degrade the reliability of most X-ray/OIR matching algorithms, because every such X-ray source is an opportunity for generating a spurious match declaration (arising from the random proximity of unrelated astrophysical objects in the two catalogs).

When matching a *Chandra* catalog to an OIR catalog, we use simulations to estimate the fraction of *Chandra* sources that have true counterparts and to statistically characterize the performance of the matching run (Broos et al. 2007, 2011). One useful product of those simulations is a quality metric for the run—the fraction of declared matches expected to be spurious. That match quality depends on the fraction of X-ray sources with true counterparts, on the size of the *Chandra* and OIR position uncertainties, and on the density of the catalogs.

We identified possible counterparts in the six OIR catalogs listed in Table 4:

1. The Gaia catalog reports optical sources across the entire T-ReX field to a limiting magnitude of $G < 21$, with effective spatial resolution comparable to ACIS (Gaia Collaboration 2018).
2. The VISTA Magellanic Cloud survey catalog (Irwin et al. 2004; Hambly et al. 2008; Cross et al. 2012, VMC;) reports near-infrared sources across the entire T-ReX field to limiting magnitudes of $Y = 21.1$, $J = 21.3$, and $K_S = 20.7$ with comparable spatial resolution to ACIS on-axis. We have used data from the 3rd data release.
3. The VLT-FLAMES Tarantula Survey (VFTS) catalog (Evans et al. 2011) is a list of 930 candidate massive stars, many subsequently confirmed via spectroscopic classification in the 30 Doradus region of the Large Magellanic Cloud (Walborn et al. 2014; Evans et al. 2015).
4. Doran et al. (2013) published a comprehensive list of known and candidate massive stars in the 30 Doradus region, with cross-references to the VFTS catalog.
5. The *Hubble* Tarantula Treasury Project (HTTP) catalog reports point-source photometry in eight visible through NIR filters for a subset of the T-ReX field (Sabbi et al. 2016). Each filter reaches a sensitivity of 25th magnitude or better, with bright-source limits ranging between magnitudes 15 and 17. The spatial resolution of *HST* is 5 to 10 times sharper than ACIS on-axis.
6. The *Spitzer* Surveying the Agents of Galaxy Evolution (SAGE Meixner et al. 2006) program cataloged mid-infrared point sources (in five filters ranging from 3/6 to 24 μm) across the LMC, including the entire T-ReX field. Point-source sensitivity ranged from $[3.6] \lesssim 18$ to $[24] \lesssim 11$, with saturation limiting the bright sources to $\gtrsim 4$ to 6 magnitudes. The angular resolution of *Spitzer* at 3.6 μm was about five times poorer than ACIS on-axis.

We performed simple experiments by which we introduced small, random positional offsets between the T-ReX catalog and OIR catalogs to assess the fraction of longer-wavelength counterparts consistent with random chance. These simulations demonstrated that within the T-ReX field the fraction of *Chandra* sources with true, one-to-one counterparts in the OIR catalogs is very low, hence producing a counterpart list with a high level of quality is very challenging. We employed two important strategies for improving counterpart quality.

The first strategy was to improve the published positions in the OIR catalogs. As shown in Table 4, we shifted the coordinate frames of the VMC, SAGE, and *Chandra* catalogs to match the Gaia

frame.²⁰ Each subgroup of massive star coordinates we obtained from Doran et al. (2013) was shifted to optimally align with the Gaia frame. Individual source positions in the VFTS and HTTP catalogs were significantly improved by constructing field distortion maps. Single-axis (α, δ) position uncertainties (column PosErr in Table 4) were estimated for the VMC, VFTS, Doran, and HTTP catalogs by examining the distribution of offsets along each coordinate axis between those catalogs and Gaia.

The second counterpart quality improvement strategy was to reduce the density of the HTTP and *Chandra* catalogs. Among the X-ray emitting objects likely to be detected by HTTP, those of most interest to us are massive stars and T-Tauri stars. Thus, we made two photometry selections designed to select those objects: a magnitude cut ($F555 < 19$) to select massive stars, and a color-magnitude selection in the F555W vs F555W-F775W diagram approximating the locus of T-Tauri stars in Figure 20 of Ksoll et al. (2018). Those selections reduced the size of the HTTP catalog from $>8 \times 10^5$ to 29,445 rows.

We found that counterpart matching quality could also be significantly improved by trimming the *Chandra* catalog using any of several X-ray properties, including detection significance, position uncertainty, off-axis angle, observed photon flux, and median energy of the extracted X-ray events. We chose to trim the *Chandra* catalog independently for matching to each OIR catalog, using the X-ray detection significance thresholds reported in footnote *h* of Table 4.

A.1. Massive Stars

Our list of known and candidate massive stars in the T-ReX field consists of the 930 bright stars in the VFTS catalog and the additional >500 massive stars that Doran et al. (2013) collected from pre-existing catalogs. Due to crowding in R136, we chose to identify X-ray counterparts in our list of known and candidate massive stars via visual review and human judgement, rather than by algorithmic catalog matching. In that visual review positions of OIR sources (VFTS, Doran, and HTTP positions, corrected as described above) and position error rectangles for our X-ray sources were displayed on an *HST* image (Sabbi et al. 2016). In most cases, we were able to identify the VFTS/Doran object in the Gaia catalog and make our counterpart decision using the Gaia position for the massive star. The median separation between OIR (often Gaia) and X-ray positions was 0.15 arcsec.

Table 5 lists the known and candidate massive stars that we judge to have been detected as individual T-ReX point sources (with the significance cut shown in Table 4, $ProbNoSrc_MostValid < 1 \times 10^{-3}$). Table 6 reports instances of close pairs or multiples of massive stars that were judged to be detected but unresolved by ACIS. These datasets were used by C22 for an in-depth study of X-ray emission from early-type stars in 30 Dor.

An additional 37 *Chandra* sources are located within 1–2'' of a VFTS/Doran source, making it tempting to believe that these massive stars were also detected in X-rays. However, we judged that the separations between these X-ray sources and the nearby massive stars were inconsistent with their position uncertainties.

²⁰ Gaia positions were propagated to the mean epoch of the *Chandra* data (Y2014.5)

Table 4. Catalog Matching Summary

Catalog		Position (α, δ)		Rows Retained		Matches	
Name	Citation	Shift	Error	OIR	<i>Chandra</i>	Gross	Correct
(1)	(2)	mas	mas	(5)	(6)	matches	% of gross
(1)	(2)	(3)	(4)	(5)	(6)	(7)	(8)
Gaia	Gaia Collaboration (2016, 2018)	<i>a</i>	published	all	497 ^{<i>h,i</i>}	114 ^{<i>k</i>}	78% ^{<i>k</i>}
VMC	Cioni et al. (2011)	(23,15)	(41,44)	all	497 ^{<i>h,i</i>}	114 ^{<i>k</i>}	78% ^{<i>k</i>}
VFTS	Evans et al. (2011)	<i>b</i>	(15,13)	all	1910 ^{<i>h</i>}	>74	...
Doran	Doran et al. (2013)	<i>c</i>	<i>d</i>	<i>f</i>	1910 ^{<i>h</i>}	>32	...
HTTP	Sabbi et al. (2016)	<i>b</i>	(2.7,4.3)	<i>g</i>	1013 ^{<i>h,i,j</i>}	124	63%
SAGE	Meixner et al. (2006)	(64,17)	(134,110)	all	851 ^{<i>h,i</i>}	79	90%
T-ReX	...	(17,23)	<i>e</i>

NOTE— Column “Shift” reports the shift applied to published coordinates to align with Gaia. “Rows Retained” reports the subset of the published catalog used for counterpart identification. Column “Gross” reports the number of possible counterparts declared. Column “Correct” reports the fraction of gross counterpart declarations that are likely to be true astrophysical counterparts, estimated via simulations.

^a Gaia positions were precessed to the mean epoch of the *Chandra* data (Y2014.5).

^b Field distortions in the coordinates reported by the HTTP and VFTS catalogs were reduced by constructing smooth field distortion maps derived from matching those catalogs to Gaia. The median (maximum) HTTP correction was 67 (1200) mas. The median (maximum) VFTS correction was 81 (160) mas.

^c Each subgroup of massive star coordinates we obtained from Doran et al. (2013)—originally from the CTIO, Parker, Selman, WFI, Walborn, Zaritsky, and De Marchi catalogs—was shifted to optimally align with the Gaia catalog.

^d Position errors were estimated for each published catalog collated by Doran et al. (2013): 0.025″ for dM, ~ 0.1 ″ for W, S, C, P catalogs.

^e For matching, a systematic error (0.08″) was added in quadrature to published *Chandra* position errors.

^f Excluded Doran sources with a published VFTS identification (Doran et al. 2013), and the following Doran sources that we believe are missing VFTS cross-identifications: VFTS416=Doran390, VFTS562=Doran778, VFTS1011=Doran533, VFTS1024=Doran683, VFTS641=Doran884, VFTS522=Doran578, VFTS468=Doran451.

^g For matching, we selected 29,445 candidate massive stars ($F555 < 19$ mag) and candidate T Tauri stars (a region of the F555W vs F555W-F775W color-magnitude diagram approximating the locus of T Tauri stars in Figure 20 of Ksoll et al. (2018)).

^h To achieve reasonable match quality (Column 8), matching used only high-significance X-ray detections defined by `ProbNoSrc_MostValid` $< 1 \times 10^{-5}$ for Gaia and VMC, `ProbNoSrc_MostValid` $< 1 \times 10^{-3}$ for VFTS and Doran, `ProbNoSrc_MostValid` $< 4 \times 10^{-4}$ for HTTP, `ProbNoSrc_MostValid` $< 1.2 \times 10^{-4}$ for SAGE.

ⁱ *Chandra* sources declared to have VFTS/Doran counterparts were excluded from automated matching with Gaia, VMC, HTTP, and SAGE (Table 7).

^j *Chandra* sources were cropped to the HTTP field of view.

^k *Chandra* sources were matched to the union of the Gaia and VMC catalogs, rather than to each independently.

A.2. Additional Counterparts

Counterparts to X-ray sources that are not suspected to be massive stars were identified via automated catalog matching, using the Gaia, VMC, trimmed HTTP, and SAGE catalogs described above. The matching criterion is defined such that, if the actual position uncertainties are as declared, then 99% of the true counterparts will be identified. Table 4 reports the X-ray detection significance thresholds used to trim the X-ray catalog for each matching exercise, the gross number of matches declared, and the expected quality of the declared matches (fraction of declared expected to be spurious) estimated from simulations. Table 7 lists the declared matches.

Table 5. Candidate and Known Massive Stars with T-ReX Detections

X-ray Source		VFTS/Doran ID, Adopted Coordinates ^a				Other Counterpart Names				Notes			
Label	NetCt ct	PhotonFlux \downarrow ph cm $^{-2}$ s $^{-1}$	E_{med}^{\dagger} keV	ID	RA	DEC	Src	Sep. b	Gaia #		VMC #	HTTPC	See also d
Declared Counterparts in VFTS Catalog													
p.L.610	22077	4.93E-5	3.2	399	05:38:33.413	-69:11:59.02	G	0.13	77456003693440	9048274	053833.417-691159.00	C22 C15	X-ray binary
L.698	7988	1.69E-5	1.6	482	05:38:40.221	-69:05:59.91	G	0.03	79659312960256		053840.214-690559.86	C22 T19	
p.L.830	1680	4.19E-6	1.4	527	05:38:42.359	-69:04:58.19	G	0.06	85564856502528	9019909	053842.351-690458.19	C22	
p.L.893	6955	1.69E-5	1.8	1025	05:38:42.903	-69:06:04.96	G	0.02	85534828237440		...	C22 T19	
p.L.1088	693	1.74E-6	1.4	617	05:38:47.522	-69:00:25.28	G	0.23	87733851287040	8944472	053847.533-690025.23	C22 T19	
p.L.1256	784	1.87E-6	2.0	695	05:38:57.072	-69:06:05.65	G	0.06	85500468567040	9018590	053857.072-690605.58	C22 T19	
Declared Counterparts in Doran13 Catalog													
p.L.296	1174	2.80E-6	1.9	185	05:37:49.039	-69:05:08.21	G	0.12	92338057418624	8986916	053749.028-690508.33	C22 T19	
p.L.812	933	2.02E-6	1.5	580	05:38:42.112	-69:05:55.33	G	0.06	85534828234496		053842.104-690555.29	C22	3 other Doran srcs (573, 577, 587) in ACIS aperture, but this is definitely the best match
p.L.867	522	1.61E-6	1.4	682	05:38:42.658	-69:06:02.91	D+	0.02			...	C22	Doran682 uses dM position
p.L.979	2180	4.70E-6	1.4	765	05:38:44.129	-69:05:56.71	G	0.03	85534828260608		053844.123-690556.63	C22	
p.L.995	74445	1.48E-4	1.8	770	05:38:44.256	-69:06:06.00	G	0.04	85534828257792	9020003	053844.252-690605.93	C22 P18	ACIS pile-up
p.L.1000	1865	4.09E-6	1.5	775	05:38:44.334	-69:05:54.72	G	0.02	85534828252672		053844.329-690554.66	C22	
p.L.1194	1233	2.90E-6	1.8	916	05:38:53.383	-69:02:00.88	G	0.1	86222022977920	8959289	053853.363-690200.88	C22 T19	

NOTE— Sources with >500 net counts are displayed above; the full table is available in the online journal. Reported properties of ACIS sources (NetCounts.t, PhotonFlux.t, MedianEnergy.t from Table 2) are derived by combining all observations. In some cases the source detection is most significant in a single observation. NetCounts suggests the quality of the extracted spectrum, but is unsuitable for photometry. Apparent Photon Flux (NetCounts / MeanEffectiveArea / ExposureTimeNominal) is a rough scaling of NetCounts to account for source-to-source variations in exposure time, effective area, and aperture size (Broos et al. 2010, Section 7.4).

^a The coordinates published in the VFTS and Doran catalogs were not directly used to assess positional coincidence between X-ray sources and candidate/known massive stars. When the star could be identified in the Gaia catalog (Src “G”), Gaia coordinates (propagated to the mean epoch of the *Chandra* data, Y2014.5) and uncertainties were adopted. Otherwise, when the star could be identified in the VMC catalog (Src “V”), VMC coordinates were adopted and uncertainties were estimated by the authors. Otherwise, published VFTS coordinates (“V+”) were corrected using a field distortion map derived using Gaia and uncertainties were estimated by the authors. Otherwise, published Doran coordinates (“D+”) were corrected using frame shifts derived using Gaia and uncertainties were estimated by the authors.

^b Separation between ACIS source and star’s Adopted Coordinates; median is 0.15 arcsec.

^c Source label in the HTTP catalog. Due to space limitations, our corrected HTTP positions are not reported.

^d Modeling of the T-ReX spectrum is described by Crowther et al. (2022, C22), Tehrani (2019, T19), Pollock et al. (2018, P18), Clark et al. (2015, C15).

Table 6. Candidate and Known Massive Stars Associated with ACIS Source Blends In R136

X-ray Source				VFTS/Doran				Notes
Label	NetCt ct	PhotonFlux ph cm ⁻² s ⁻¹	E_{med} keV	ID	Src	Sep.	See also	
p1.987	84	1.96E-7	1.2	V1034 ^a	G	0.2	C22	Both could contribute to ACIS light
				D772	D+	0.3		
p1.866	62	1.50E-7	1.4	D685	G	0.25	C22	Both could contribute to ACIS light
				D671	D+	0.5		
p1.832	4452	1.15E-5	1.5	D633	D+		C22 T19	Mushroom aperture at ACIS aimpoint; hopelessly confused at R136 core
				D630	D+			
				D642	D+			
				D638	D+			
p1.766	31	9.70E-8	1.6	V513 ^b	G	0.2	C22	Both could contribute to ACIS light
				V515	V+	0.4		
cc4970	496	2.39E-6	1.7	D613	D+		C22 T19	~8 Doran srcs in ACIS aperture
				D621	D+			
c7182	258	6.18E-7	1.4	D657	D+		C22	Many Doran sources in ACIS aperture
				D652	D+			
				D649	D+			
				D659	D+			
c7157	345	8.16E-7	1.3	D648	D+		C22	Many Doran sources in ACIS aperture
				D624	D+			
c7018	45	2.20E-7	1.5	D589	D+		C22	Many Doran sources in ACIS aperture
				D583	D+			

NOTE—See footnotes to Table 5.

^a We suspect that the identifiers VFTS1034 and Doran769 refer to the same star.^b We suspect that the identifiers VFTS513 and Doran558 refer to the same star.

Table 7. Counterparts To X-ray Sources Beyond the Massive Stellar Population

X-ray Source		Gaia+VMC			HTTP d			SAGE			SIMBAD C					
Label	PosErr	b	Gaia ID	VMC ID	K	Dist.	b	ID	Shift	F555	Dist.	b	SAGE ID	3.6 μ m	SIMBAD C	
"	"	"	#4657	#55834	mag	"	"	"	mas	mag	"	"	"	mag	"	
pL255																Pulsar (PSR J0537-6910)
pass52.4																Rotationally variable Star (HD 269921)
pL1548	0.2	0.4	783116463742336	8880341	10	0.2	0.2	053955.602-690846.62	130.688	25		0.2	J053939.44-690029.7	14	AGN ([GC2009] J053939.48-690030.0)	
pL1529	0.2	0.1	684980764259456	8944793	16							0.1	J053938.25-685740.2	14	YSO (2MASS J05393821-6857404)	
c11125	0.3	0.2	8919503	8919503	15	0.3	0.3	053935.478-690438.90	204.381	17		0.4	J053935.50-690438.6	12		
pL1521	0.1	0.2	682923488239360	9014587	13							0.5	J053933.97-691130.4	16		
pL1517	0.2	0.3		9778551	20											
c10740	0.3	0.5		9713682	18	0.2	0.2	053925.779-691031.35	-28,-54	23		0.2	J053915.91-685752.2	17		
c10422	0.2	0.2		9768044	18							0.6	J053915.91-685950.0	15		
pL1420	0.2	0.3		8939594	16							0.1	J053914.96-690923.7	14	Long-period variable star (2MASS J05391496-6909238)	
c10393	0.2	0.1	679281354744320	9023693	14	0.1	0.1	053914.961-690923.81	-20,-139	19						
c10370	0.2	0.1		9767609	19							0.1	J053913.96-685728.6	17		
c10266	0.1	0.2	679384433817472	9014737		0.2	0.2	053910.764-690756.78	10,-129	18		0.4	J053910.79-690756.7	15		
pL1368	0.1	0.1		9706871	18							0.1	J053908.45-685958.6	16		
pL1317	0.0	0.0		9774684	21	0.0	0.0	053903.176-690703.87	24,-125	24		0.4	J053859.69-685949.3	17		
c9590	0.2	0.3		8938310	18							0.3	J053856.83-685636.3	15		
c9506	0.4	0.3		8849680	17							0.3	J053859.31-684959.5	15		
pL1246	0.2	0.4	688416745861760	8912946	17							0.2	J053848.73-690715.6	15		
c9209	0.1	0.1		8978864		0.1	0.1	053856.710-690426.29	42,-84	22		0.4	J053848.05-690210.8	16		
c8790	0.1	0.2		9707745	18							0.2	J053846.84-690505.4	10		
cc5713	0.1	0.1		9770921	18							0.5	J053845.63-685759.7	17		
c8315	0.1	0.3				0.4	0.4	053848.720-690715.56	27,-94	23		0.4	J053843.50-690629.0	14	YSO (OGLE LMC-ECL-21448)	
c8216	0.1	0.1				0.2	0.2	053846.871-690505.58	38,-73	24						
pL1056	0.2	0.2		8921036	18							0.2	J053852.25-690126.9	17		
c7568	0.1	0.1		8996929	17	0.2	0.2	053843.546-690628.82	33,-69	18		0.4	J053848.73-690715.6	15		
c6236	0.1	0.2		9774528	17	0.2	0.2	053839.963-690652.52	33,-54	26		0.4	J053848.05-690210.8	16		
c6150	0.1	0.0	685534828103552			0.0	0.0	053839.633-690532.25	39,-48	17		0.2	J053846.84-690505.4	10		
c5895	0.1	0.2	679659312977664			0.2	0.2	053838.549-690612.85	35,-45	17		0.4	J053843.50-690629.0	14		
c5836	0.3	0.5		9705089	17							0.7	J053837.20-685655.0	16		
pL641	0.2	0.2		9767536	19							0.3	J053836.65-685725.9	18		
pL639	0.1	0.2		9038525		0.2	0.2	053836.577-691056.66	-14,-38	22						
pL609	0.3	0.7		8923829	18							0.3	J053833.49-685817.9	17		
c5204	0.2	0.0		8968459		0.1	0.1	053832.322-690314.89	14,-9	22						
pL574	0.1	0.2		9707046	18							0.4	J053826.21-690012.9	16		
c4405	0.4	0.7	783490104306304	8855976	10							0.9	J053821.25-685034.0	10		
c3916	0.2	0.3	686698750750848	8976411		0.3	0.3	053810.121-690224.70	14.80	19						
pL464	0.2	0.3	688863422482304	8912592	16							0.2	J053809.91-685657.7	15		
c3775	0.2					0.6	0.6	053806.273-691310.00	-37.46	24		0.8	J053806.27-691310.1	15		
c3766	0.2	0.2	679968549406848	9021508	13	0.2	0.2	053805.644-690909.77	13.70	19		0.3	J053805.61-690909.6	11	YSO (2MASSX J05380564-6909098)	

Table 7 continued on next page

Table 7 (continued)

X-ray Source Label	PosErr "	b		Gaia+VMC		b		HTTP ^a		SAGE		SIMBAD ^C	
		Dist.	"	Gaia ID #4657	VMC ID #55834	K mag	Dist.	"	ID	Shift mas	F555 mag		Dist. "
p1_450	0.0	0.1	0.1	9708672	19	0.1	053802.741-690259.15	24,105	22	0.1	J053802.75-690258.9	16	
c3526	0.2	0.6	0.6	8872736	17					0.7	J053757.84-685238.2	16	
p1_410	0.1	0.3	0.2	9710167	16	0.2	053754.561-690516.57	23,107	26				
p1_406	0.1	0.1	0.1	9771021	20								
e2202	0.5	0.5	0.5	701198560089088	17							AGN (MQS J053745.77-685311.4)	
c1348	0.5	0.6	0.6	9705614	16								
c1167	0.2	0.5	0.5	692024485433088	16								
p1_11	0.2	0.2	0.2	9711726	17	0.2	053725.617-690738.37	-12,29	25	0.4	J053725.55-690738.2	16	
c1042	0.3		0.3			0.3	053721.382-690621.28	-13,11	26	0.6	J053721.45-690621.4	17	
c979	1.1	1.9	1.9	663849561921024	9131446					1.5	J053714.70-692021.0	17	
c919	0.3	0.2	0.2	690001595436160	9033573	0.2	053710.840-691025.19	49,51	18	0.4	J053710.87-691025.1	14	
p1_5	0.3	0.4	0.4	690070295111040	9025732	18				0.5	J053703.80-690942.6	17	
c749	0.4	0.7	0.7	693433288582784	8962789	16				0.6	J053658.57-690234.2	16	
pass53_1	0.2	0.3	0.3	666323458738560	9061522	15	0.3	053657.042-691328.57	309,290	21	0.1	J053657.42-691328.2	14
c373	0.9	0.8	0.8	702989558190336	8894623	14				0.8	J053612.44-685455.9	14	
c73	0.2	0.5	0.5	9090770	15							SNR.1987A	

NOTE—A portion of this table, highlighting sources with counterparts in more than one optical/IR catalog, is provided here to illustrate format and content. The full table is available in the online journal.

^a Column "ID" is the published label for a detection in the HTTP catalog. Column "Correction" reports the shift we applied to the published position.

^b Separation between ACIS source and Adopted Coordinates.

^c Identifiers reported by SIMBAD.

^d Using our judgement, we assert two associations that were not found by automated methods: Pulsar PSR J053747.40-691020.2 (p1_255); the low-mass star HD 269921 == T-ReX 053834.66-685306.1 (pass52.4).

B. HIGH-QUALITY VARIABLE SOURCES

In this Appendix we briefly highlight several striking, high-quality variable sources. This is by no means an exhaustive list, and we would expect the T-ReX catalog to provide a resource for various future variability studies.

B.1. *Periodic Variation*

Binary stellar systems can exhibit periodic modulation of the unresolved X-ray emission from the system, due to time-varying accretion, eclipses, or time-variation in the physical state of colliding winds. The long-baseline T-ReX observations (Table 1) provide several high-quality examples of periodic variation.

The multipanel figure sets below (Figures 13, 15, and 16) depict X-ray lightcurves (representing a 68% confidence interval versus phase), phase-folded median X-ray energy, and periodograms. The phase-folded lightcurves were constructed for the specified period by converting X-ray event timestamps (with barycentric correction) to phase values, calculating the phase distribution of those phased events, calculating the phase distribution of all the time periods in which the source was observed (using *CIAO*'s Good Time Interval data product), and then adaptively smoothing the event and exposure distributions to achieve a signal-to-noise goal. The result is a smooth estimate of gross (star plus background) photon flux (in units of $\text{photon s}^{-1} \text{cm}^{-2}$) with uncertainties. The median energy time-series were constructed by simply binning the phased events, calculating the median energy of the events in each bin, and estimating uncertainties (employing a binomial distribution).

The periodograms plot p -values for the Kuiper statistic, under the null hypothesis of a constant flux, computed on the phased event distribution and the phased exposure distribution (Paltani 2004) for a large number of trial periods. Sharp local minima in the periodogram suggest periodic variability, however interpretation requires caution because interactions between the observational sampling and aperiodic variability of the source can also produce small p -values.

R144

The binary Wolf-Rayet star R144 (053853.36-690200.9, p1_1194, Doran 916) has a published optical period of 74.2074 day (Shenar et al. 2021), which is consistent with the period we estimate from the T-ReX data (~ 74.4 day, Fig. 13). When folded on that optical period, R144 exhibits $\sim 50\%$ X-ray flux modulation (Shenar et al. 2021, Fig. 17) and clear modulation of the apparent spectral hardness (Fig. 13).

Before modeling the phase-resolved X-ray spectrum of R144, we first identified a reasonable model for the complete spectrum (full ~ 2 Ms exposure), consisting of two thermal plasmas with independent absorbers (in *XSPEC*, the model $tbvarabs1*vapec1 + tbvarabs2*vapec2$). That fit indicated plasma temperatures of 0.74 and 2.1 keV. One possible interpretation of this model would be a soft plasma produced by each of the stars plus a hard plasma produced by a colliding wind shock.

We then fit spectra obtained from ten groups of observations with similar phase (Table 8). Each group contains 3–10 ObsIDs. We investigated the simple hypothesis that the observed variation was dominated by only one phase-dependent parameter, the absorption (N_{H2}) of the colliding wind shock emission (kT_2). Specifically, each of the ten phase-resolved spectra was fit with kT_1, kT_2 and N_{H1} frozen to the values obtained from the models of the complete spectrum. N_{H2} and the plasma normalizations remained free parameters. Most of the phase-interval spectra were well-fit by this

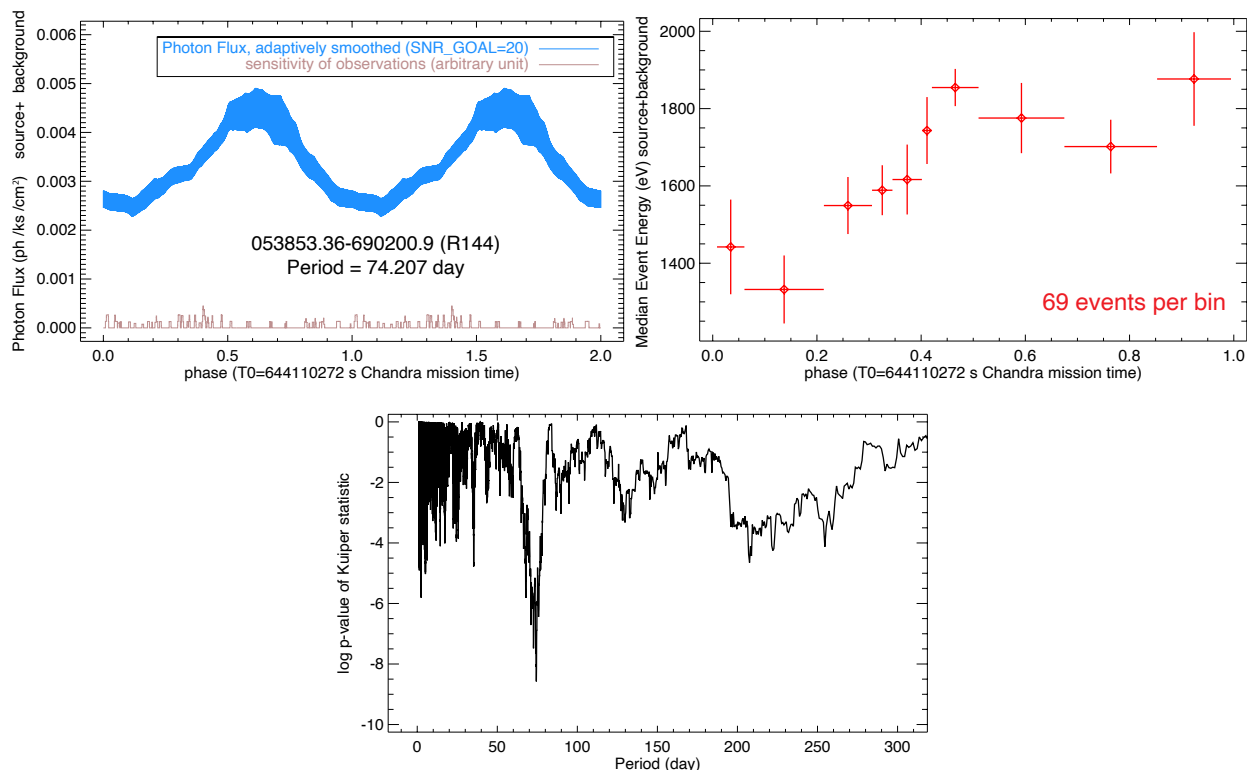


Figure 13. Phase-dependent X-ray flux (*top left*) and median X-ray event energy (*top right*) for R144 (053853.36-690200.9, p1_1194, Doran 916). Phase is calculated for a published optical period (74.2074 day) and T0 (periastron, MJD 58268.98; [Shenar et al. 2021](#)). A similar period estimate (~ 74.4 day) was obtained from the X-ray data (*bottom*).

model (see χ^2_ν in Table 8). Under these model assumptions, the phase modulations of N_{H2} and the absorption-corrected luminosities are plotted in Figure 14.

R145

The binary Wolf-Rayet star R145 (053857.06-690605.6, p1_1256, VFTS 695) has a published optical period of 158.76 day ([Schnurr et al. 2009](#); [Shenar et al. 2017](#)), which is consistent with the T-ReX data ([Tehrani 2019](#)). When folded on that period, we find that R145 exhibits $\sim 80\%$ X-ray flux modulation and clear modulation of the apparent spectral hardness (Fig. 15).

R139

The T-ReX data for the O6.5I+O6I binary R139 (053842.34-690458.1, p1_830, VFTS 527) exhibit $\sim 65\%$ X-ray flux modulation and clear modulation of the apparent spectrum when folded on the period we estimate from the T-ReX data (~ 153.0 day, Fig. 16). This period is very similar to the 153.90-day period derived from optical radial velocity measurements ([Taylor et al. 2011](#)).

Mk33Na

Periodic variation of the O3If ([Massey & Hunter 1998](#)) star Mk33Na (053844.33-690554.7, p1_1000, Doran 775, Hunter 16, MUSE 1943) has been detected in both the T-ReX data ($P \sim 18.3$ day) and

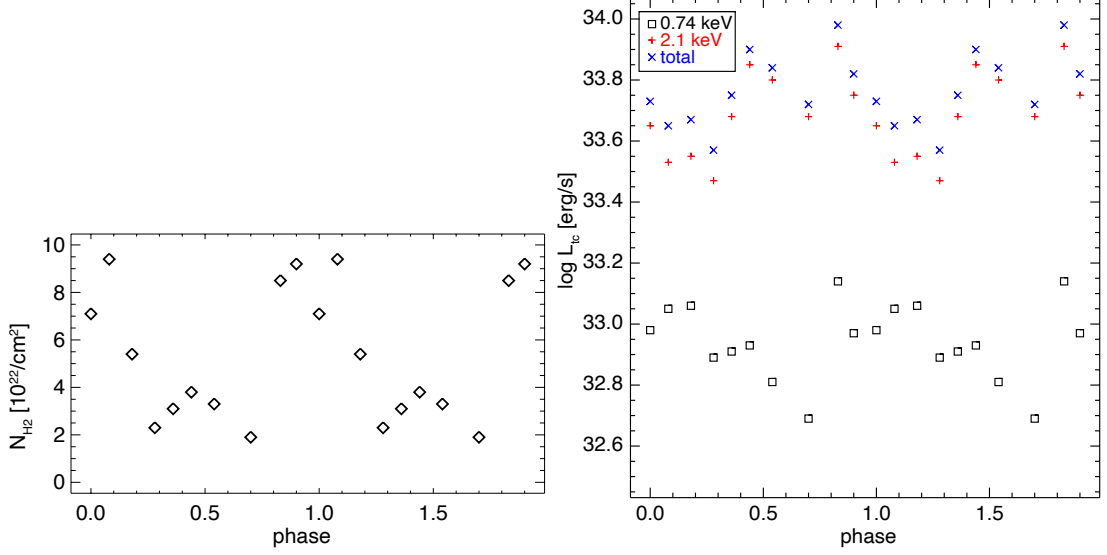


Figure 14. Phase modulation of the hot plasma absorption (left) and absorption-corrected luminosity (right) in a model of the R144 spectrum.

Table 8. R144 ACIS X-ray Spectroscopy for Ten Phase Intervals

phase ^a	Spectral Fit ^b								X-ray Luminosities ^c						
	χ^2_ν	N_{H1}	A_{V1}	kT_1	$EM1$	N_{H2}	A_{V2}	kT_2	$EM2$	L_{1t}	L_{1tc}	L_{2t}	L_{2tc}	L_t	L_{tc}
		(10^{22}cm^{-2})	(mag)	(keV)	($\log \text{cm}^{-3}$)	(10^{22}cm^{-2})	(mag)	(keV)	($\log \text{cm}^{-3}$)	(log erg s ⁻¹)					
R144, D=50.0 kpc															
p00	1.11	0.452*	0.7	0.74*	56.1 ^{+0.2} _{-0.3}	7.1 ^{+4.7} _{-3.4}	10.9	2.1*	56.7 ^{+0.2} _{-0.2}	32.73	32.98	33.14	33.65	33.28	33.73
p08	1.59	0.452*	0.7	0.74*	56.1 ^{+0.1} _{-0.2}	9.4 ^{+8.8} _{-3.9}	14.4	2.1*	56.6 ^{+0.2} _{-0.2}	32.80	33.05	32.95	33.53	33.18	33.65
p18	0.58	0.452*	0.7	0.74*	56.2 ^{+0.1} _{-0.2}	5.4 ^{+4.9} _{-3.1}	8.4	2.1*	56.6 ^{+0.2} _{-0.2}	32.81	33.06	33.08	33.55	33.27	33.67
p28	1.04	0.452*	0.7	0.74*	56.0 ^{+0.2} _{-0.5}	2.3 ^{+1.5} _{-1.0}	3.5	2.1*	56.6 ^{+0.1} _{-0.1}	32.63	32.89	33.15	33.47	33.27	33.57
p36	0.40	0.452*	0.7	0.74*	56.0 ^{+0.2} _{-0.3}	3.1 ^{+1.1} _{-0.9}	4.7	2.1*	56.8 ^{+0.08} _{-0.09}	32.66	32.91	33.32	33.68	33.40	33.75
p44	1.15	0.452*	0.7	0.74*	56.0 ^{+0.2} _{-0.6}	3.8 ^{+1.6} _{-1.3}	5.8	2.1*	56.9 ^{+0.09} _{-0.11}	32.68	32.93	33.45	33.85	33.52	33.90
p54	1.23	0.452*	0.7	0.74*	55.9 ^{+0.3} _{...}	3.3 ^{+2.0} _{-1.5}	5.1	2.1*	56.9 ^{+0.1} _{-0.1}	32.55	32.81	33.42	33.80	33.48	33.84
p70	0.86	0.452*	0.7	0.74*	55.8 ^{+0.4} _{...}	1.9 ^{+2.2} _{-1.3}	2.9	2.1*	56.8 ^{+0.2} _{-0.2}	32.43	32.69	33.39	33.68	33.44	33.72
p83	1.15	0.452*	0.7	0.74*	56.2 ^{+0.1} _{-0.2}	8.5 ^{+7.2} _{-4.4}	13.1	2.1*	57.0 ^{+0.2} _{...}	32.88	33.14	33.36	33.91	33.49	33.98
p90	0.94	0.452*	0.7	0.74*	56.1 ^{+0.1} _{-0.2}	9.2 ^{+5.2} _{-3.4}	14.2	2.1*	56.8 ^{+0.1} _{-0.2}	32.71	32.97	33.18	33.75	33.31	33.82

^aPhase groups are labeled, for example, with “p36” representing the spectrum obtained by merging a group of observations with phase ~ 0.36 .

^bAll fits used the thermal plasma model $tbvarabs*vapec+tbvarabs*vapec$ with abundances for both absorption and plasma components as adopted by Tehrani (2019). Best-fit values for the extinction are shown both as a column density and as $A_V = N_H/6.5 \times 10^{21} \text{cm}^{-2}$. Quantities marked with an asterisk (*) were frozen in the fit. Uncertainties represent 90% confidence intervals. Uncertainties are missing when XSPEC was unable to compute them or when their values were so large that the parameter is effectively unconstrained.

^cX-ray luminosities in the total (t) band (0.5–8 keV) are derived from the model spectrum, assuming a distance of 50 kpc. Absorption-corrected luminosities are subscripted with a c. Model luminosities may underestimate the true X-ray luminosity for sources with high absorption because an additional soft thermal plasma could be present but unmeasurable in the X-ray spectrum.

in optical spectra obtained over a short baseline ($P=18.32 \pm 0.14$ day Bestenlehner et al. 2022). When folded on that period, the T-ReX data exhibit flux modulation of $\sim 50\%$ and modulation of

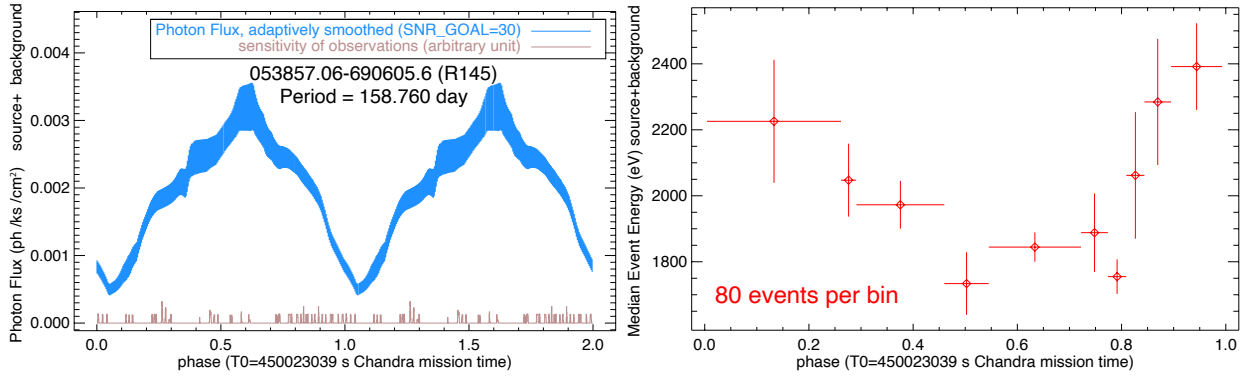


Figure 15. Phase-dependent X-ray flux (left) and median X-ray event energy (right) for R145 (053857.06-690605.6, p1_1256, VFTS 695). Phase is calculated for a published optical period (158.76 day) and T0 (MJD 56022.6) (Schnurr et al. 2009; Shenar et al. 2017).

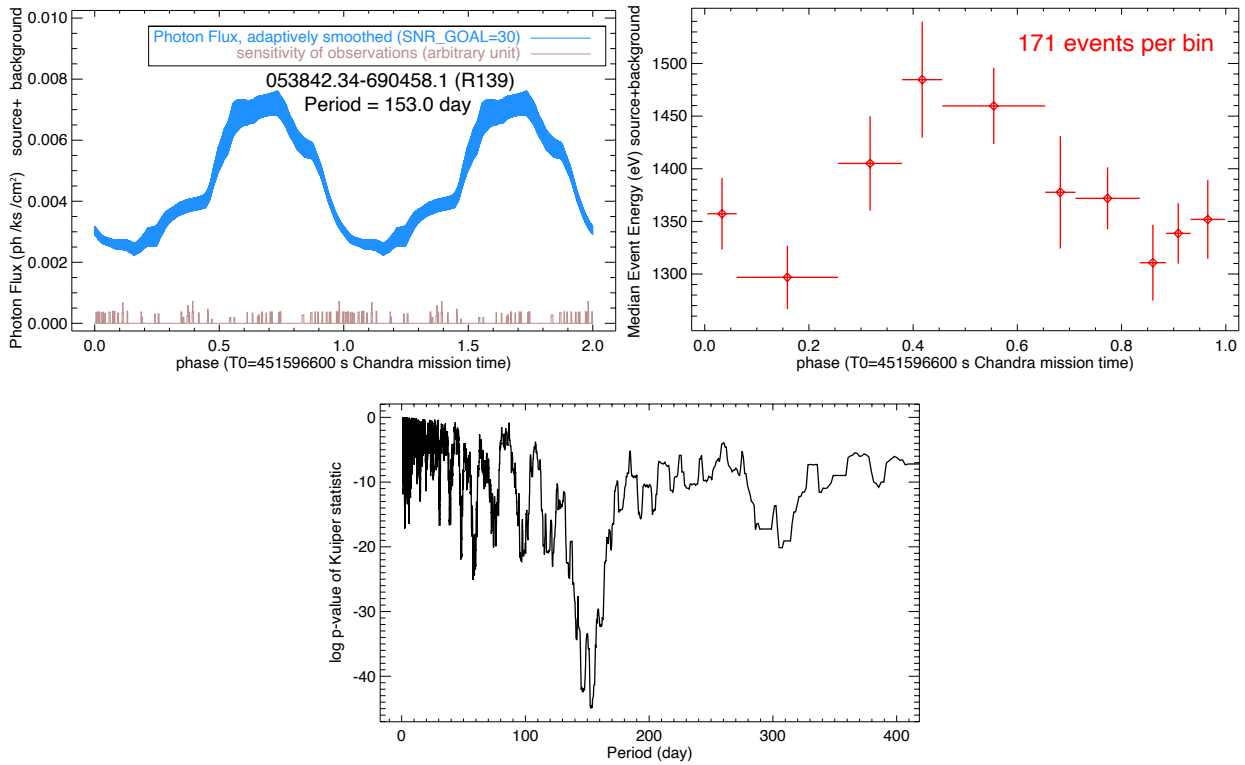


Figure 16. Phase-dependent X-ray flux (left) and median X-ray event energy (right) for R139 (053842.34-690458.1, p1_830, VFTS 527). Phase is calculated for the period we estimate from the T-ReX data (~ 153.0 day, bottom). T0 is derived from optical data (MJD 56041.3125, Hugues Sana, private communication).

the apparent spectrum consistent with a phase-dependent absorbing column density (Bestenlehner et al. 2022).

VFTS 399

Clark et al. (2015) discovered that the massive (O9) star VFTS 399 (053833.43-691159.0, p1_610)

probably has an accreting neutron star companion, based in part on the ~ 2567 s periodic modulation found in its T-ReX lightcurve.

Mk34

Pollock et al. (2018) find that Mk34 (053844.25-690605.9, p1_995, VFTS 770) is an eccentric colliding-wind Wolf-Rayet binary system with a period of ~ 155 days, based on its remarkable T-ReX lightcurve.

Mk39

Tehrani (2019, Chapter 4) estimate the period (~ 640 day) of the binary Wolf-Rayet star Mk39 (053840.22-690559.8, p1_698, VFTS 482) using the T-ReX data.

B.2. “Flares”

Fast-rise, slow-decay “flares” were seen in at least two foreground stars. The low-mass star HD 269921²¹ (053834.66-685306.1, pass52_4) shows variability by a factor of ~ 100 (Figure 17). Moór et al. (2013) report a spectral type of G7V, and assert membership in the Columba moving group. These data (85,000 X-ray events) should allow time-resolved spectroscopy of the two complete “flare” events observed, which exhibit spectral hardening (red curve).

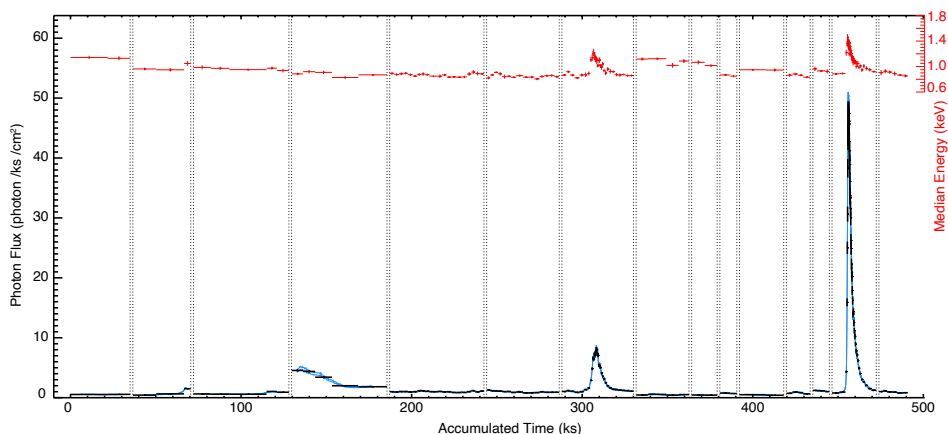


Figure 17. HD 269921 (053834.66-685306.1, pass52_4) lightcurve (blue, with grouped events in black) and median energy timeseries (red). Two complete “flare” events exhibit spectral hardening. Vertical dotted lines mark the boundaries of individual ObsIDs.

The foreground star VFTS 2077²² (053935.54-690438.2, p1_1521) shows dramatic variability in two of its 54 observations (Figure 18). The peak count rate at the end of ObsID 16446 (0.038 ct/s = 29 counts in a 770 s interval) is 460 times the mean count rate (8×10^{-5} ct/s = 169 net counts in 2 Ms).

Finally, the foreground low-mass star CAL 69²³ (053816.28-692331.1, c4107) is an early M dwarf (Riaz et al. 2006) exhibiting complex, frequent flaring activity (Figure 19). Obtaining this long-baseline lightcurve for this star was serendipitous, as it happened to fall within the extreme southern

²¹ 94 pc, Gaia DR2 4657783116463742336 (0.47'' separation)

²² 220 pc, Gaia DR2 4657682923488239360 (0.2'' separation)

²³ 53 pc, Gaia DR3 4657651793560005632 (1.33'' separation at large off-axis angle)

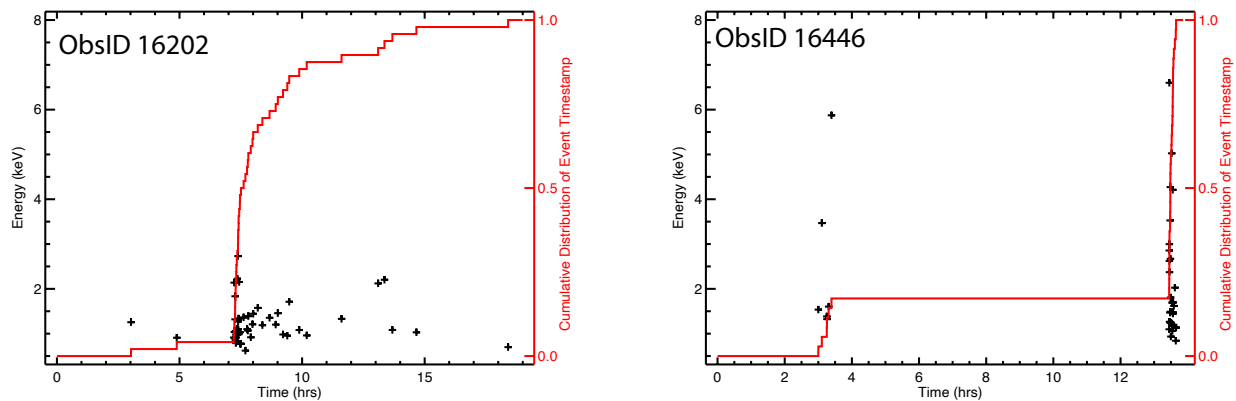


Figure 18. Flares within two single ObsIDs of foreground source 053935.54-690438.2 (p1_1521). Black + symbols depict the arrival time and energy of individual events, while the red curves give the cumulative distributions of arrival times. The p -values for the null hypothesis (constant flux) are 1×10^{-5} and 3×10^{-21} for ObsIDs 16202 and 16446, respectively.

portion of the T-ReX field (Figure 2). X-ray activity in low-mass stars provides an important constraint on exoplanet habitability models.

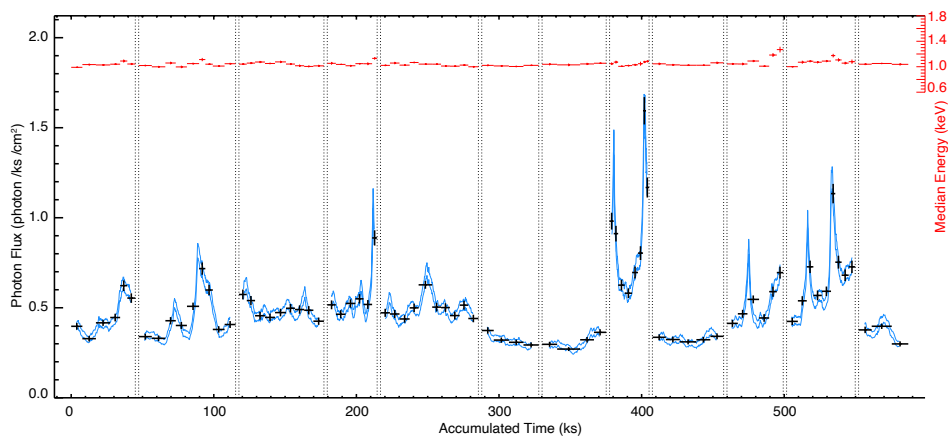


Figure 19. CAL 69 (053816.28-692331.1, c4107) lightcurve, plotted with symbols and axes as in Figure 17. Frequent, low-amplitude flares are observed, with evidence for spectral hardening.

REFERENCES

- Albacete-Colombo, J. F., Drake, J. J., Flaccomio, E., et al. 2023, *ApJS*, 269, 14.
doi:10.3847/1538-4365/acdd65
- Alexander, D. M., Bauer, F. E., Brandt, W. N., et al. 2003, *AJ*, 126, 539. doi:10.1086/376473
- Anders, E., & Grevesse, N. 1989, *GeoCoA*, 53, 197
- Arnaud, K. A. 1996, in *ASP Conf. Ser.* 101, *Astronomical Data Analysis Software & Systems V*, ed. G. H. Jacoby & J. Barnes (San Francisco, CA: ASP), 17
- Bailer-Jones, C. A. L., Rybizki, J., Fouesneau, M., Mantelet, G., & Andrae, R. 2018, *AJ*, 156, 58
- Barger, A. J., Cowie, L. L., Capak, P., et al. 2003, *AJ*, 126, 632. doi:10.1086/376843
- Bastian, N., Ercolano, B., Gieles, M., et al. 2007, *MNRAS*, 379, 1302
- Bestenlehner, J. M., Crowther, P. A., Broos, P. S., et al. 2022, *MNRAS*, 510, 6133.
doi:10.1093/mnras/stab3521
- Binder, B. A. & Povich, M. S. 2018, *ApJ*, 864, 136. doi:10.3847/1538-4357/aad7b2
- Broos, P. S., Feigelson, E. D., Townsley, L. K., et al. 2007, *ApJS*, 169, 353
- Broos, P. S., Townsley, L. K., Feigelson, E. D., et al. 2010, *ApJ*, 714, 1582
- Broos, P. S., Townsley, L. K., Feigelson, E. D., et al. 2011, *ApJS*, 194, 2
- Broos, P. S., Townsley, L. K., Getman, K. V., Bauer, F. E. 2012, *AE: ACIS Extract, Astrophysics Source Code Library*, ascl:1203.001
- Broos, P. S., Getman, K. V., Povich, M. S., et al. 2013, *ApJS*, 209, 32
- Broos, P. S., & Townsley, L. K. 2016, *ACIS Extract software package*, Zenodo,
doi:10.5281/zenodo.781433
- Canizares, C. R., Davis, J. E., Dewey, D., et al. 2005, *PASP*, 117, 1144
- Chen, Y., Wang, Q. D., Gotthelf, E. V., et al. 2006, *ApJ*, 651, 237. doi:10.1086/507017
- Chen, W.-A., Li, C.-J., Chu, Y.-H., et al. 2023, *AJ*, 166, 204. doi:10.3847/1538-3881/acff72
- Cheng, Y., Wang, Q. D., & Lim, S. 2021, *MNRAS*, 504, 1627. doi:10.1093/mnras/stab1040
- Cignoni, M., Sabbi, E., van der Marel, R. P., et al. 2015, *ApJ*, 811, 76.
doi:10.1088/0004-637X/811/2/76
- Cioni, M.-R. L., Clementini, G., Girardi, L., et al. 2011, *A&A*, 527, A116
- Clark, J. S., Bartlett, E. S., Broos, P. S., et al. 2015, *A&A*, 579, A131
- Conti, P. S., Crowther, P. A., & Leitherer, C. 2012, *From Luminous Hot Stars to Starburst Galaxies*, by Peter S. Conti, Paul A. Crowther, Claus Leitherer, Cambridge, UK: Cambridge University Press, 2012
- Cross, N. J. G., Collins, R. S., Mann, R. G., et al. 2012, *A&A*, 548, A119
- Crowther, P. A. & Dessart, L. 1998, *MNRAS*, 296, 622. doi:10.1046/j.1365-8711.1998.01400.x
- Crowther, P. A., Schnurr, O., Hirschi, R., et al. 2010, *MNRAS*, 408, 731.
doi:10.1111/j.1365-2966.2010.17167.x
- Crowther, P. A., Broos, P. S., Townsley, L. K., et al. 2022, *MNRAS*, 515, 4130.
doi:10.1093/mnras/stac1952 (C22)
- Dale, J. E., Haworth, T. J., & Bressert, E. 2015, *MNRAS*, 450, 1199
- Davis, J. E., Bautz, M. W., Dewey, D., et al. 2012, *Proc. SPIE*, 8443, 84431A
- Diehl, S., & Statler, T. S. 2006, *MNRAS*, 368, 497
- Doran, E. I., Crowther, P. A., de Koter, A., et al. 2013, *A&A*, 558, A134
- Elmegreen, B. G. 2008, *ApJ*, 672, 1006
- Evans, I. N., Primini, F. A., Glotfelty, K. J., et al. 2010, *ApJS*, 189, 37
- Evans, C. J., Taylor, W. D., Hénault-Brunet, V., et al. 2011, *A&A*, 530, A108
- Evans, C. J., Kennedy, M. B., Dufton, P. L., et al. 2015, *A&A*, 574, A13.
doi:10.1051/0004-6361/201424414
- Everett, J. E. & Churchwell, E. 2010, *ApJ*, 713, 592. doi:10.1088/0004-637X/713/1/592
- Feigelson, E. D., Townsley, L. K., Broos, P. S., et al. 2013, *ApJS*, 209, 26
- Feigelson, E. D. 2018, in *The Birth of Star Clusters*, ed. S. Stahler (Cham: Springer), *ASSL*, 424, 119
- Fruscione, A., et al. 2006, *Proc. SPIE*, 6270, 62701V
- Gaia Collaboration, Prusti, T., de Bruijne, J. H. J., et al. 2016, *A&A*, 595, A1
- Gaia Collaboration, Brown, A. G. A., Vallenari, A., et al. 2018, *A&A*, 616, A1
- Garmire, G. P., Bautz, M. W., Ford, P. G., Nousek, J. A., & Ricker, G. R., Jr. 2003, *Proc. SPIE*, 4851, 28

- Getman, K. V., Flaccomio, E., Broos, P. S., et al. 2005, *ApJS*, 160, 319
- Getman, K. V., Feigelson, E. D., Broos, P. S., Townsley, L. K., & Garmire, G. P. 2010, *ApJ*, 708, 1760
- Getman, K. V., Broos, P. S., Feigelson, E. D., et al. 2011, *ApJS*, 194, 3
- Getman, K. V., Feigelson, E. D., Kuhn, M. A., et al. 2014, *ApJ*, 787, 108.
doi:10.1088/0004-637X/787/2/108
- Getman, K. V., Broos, P. S., Kuhn, M. A., et al. 2017, *ApJS*, 229, 28
- Getman, K. V. & Feigelson, E. D. 2021, *ApJ*, 916, 32. doi:10.3847/1538-4357/ac00be
- Getman, K. V., Feigelson, E. D., Garmire, G. P., et al. 2022, *ApJ*, 935, 43.
doi:10.3847/1538-4357/ac7c69
- Gotthelf, E. V. 2003, *ApJ*, 591, 361.
doi:10.1086/375124
- Gregory, S. G., Adams, F. C., & Davies, C. L. 2016, *MNRAS*, 457, 3836
- Gu, L. & Shah, C. 2023, arXiv:2301.11335.
doi:10.48550/arXiv.2301.11335
- Güdel, M., et al. 2007, *A&A*, 468, 353
- Hambly, N. C., Collins, R. S., Cross, N. J. G., et al. 2008, *MNRAS*, 384, 637
- Irwin, M. J., Lewis, J., Hodgkin, S., et al. 2004, *Proc. SPIE*, 411
- Joye, W. A., & Mandel, E. 2003, in *ASP Conf. Ser. 295, Astronomical Data Analysis Software and Systems XII*, ed. H. E. Payne, R. I. Jedrzejewski, & R. N. Hook (San Francisco, CA: ASP), 489
- Kashi, A., Principe, D. A., Soker, N. & Kastner, J. H. *ApJ*, 914, 1
- Katsuda, S., Tsunemi, H., Mori, K., et al. 2011, *ApJ*, 730, 24. doi:10.1088/0004-637X/730/1/24
- Kavanagh, P. J., Sasaki, M., Bozzetto, L. M., et al. 2015, *A&A*, 573, A73.
doi:10.1051/0004-6361/201424354
- Kim, D.-W., Wilkes, B. J., Green, P. J., et al. 2004, *ApJ*, 600, 59. doi:10.1086/379820
- Kuhn, M. A., Getman, K. V., Broos, P. S., Townsley, L. K., & Feigelson, E. D. 2013, *ApJS*, 209, 27
- Liu, J., Wang, Q. D., & Mao, S. 2012, *MNRAS*, 420, 3389. doi:10.1111/j.1365-2966.2011.20263.x
- Lopez, L. A., Krumholz, M. R., Bolatto, A. D., et al. 2011, *ApJ*, 731, 91.
doi:10.1088/0004-637X/731/2/91
- Luo, B., Bauer, F. E., Brandt, W. N., et al. 2008, *ApJS*, 179, 19. doi:10.1086/591248
- Maíz Apellániz, J., Sota, A., Arias, J. I., et al. 2016, *ApJS*, 224, 4
- Ksoll, V. F., Gouliermis, D. A., Klessen, R. S., et al. 2018, *MNRAS*, 479, 2389
- Marshall, F. E., Gotthelf, E. V., Zhang, W., et al. 1998, *ApJL*, 499, L179. doi:10.1086/311381
- Massey, P., & Hunter, D. A. 1998, *ApJ*, 493, 180
- Meaburn, J. 1980, *MNRAS*, 192, 365.
doi:10.1093/mnras/192.3.365
- Meixner, M., Gordon, K. D., Indebetouw, R., et al. 2006, *AJ*, 132, 2268. doi:10.1086/508185
- Moór, A., Szabó, G. M., Kiss, L. L., et al. 2013, *MNRAS*, 435, 1376
- Nugis, T. & Lamers, H. J. G. L. M. 2000, *A&A*, 360, 227
- Nuñez, E. H., Povich, M. S., Binder, B. A., et al. 2021, *AJ*, 162, 153.
doi:10.3847/1538-3881/ac0af8
- Paltani, S. 2004, *A&A*, 420, 789
- Park, S., Hughes, J. P., Slane, P. O., et al. 2010, *ApJ*, 710, 2
- Pellegrini, E. W., Baldwin, J. A., & Ferland, G. J. 2011, *ApJ*, 738, 34.
doi:10.1088/0004-637X/738/1/34
- Pietrzyński, G., Graczyk, D., Gallenne, A. et al. 2019, *Nature*, 567, 200.
doi:10.1038/s41586-019-0999-4
- Pollock, A. M. T., Crowther, P. A., Tehrani, K., et al. 2018, *MNRAS*, 474, 3228
- Povich, M. S., Stone, J. M., Churchwell, E., et al. 2007, *ApJ*, 660, 346. doi:10.1086/513073
- Povich, M. S., Churchwell, E., Bieging, J. H., et al. 2009, *ApJ*, 696, 1278.
doi:10.1088/0004-637X/696/2/1278
- Povich, M. S., Smith, N., Majewski, S. R., et al. 2011, *ApJS*, 194, 14
- Povich, M. S., Maldonado, J. T., Nuñez, E. H., et al. 2019, *ApJ*, 881, 37.
doi:10.3847/1538-4357/ab26b2
- Possenti, A., Cerutti, R., Colpi, M., et al. 2002, *A&A*, 387, 993. doi:10.1051/0004-6361:20020472
- Preibisch, T., Kim, Y.-C., Favata, F., et al. 2005, *ApJS*, 160, 401
- Ranalli, P., Comastri, A., Origlia, L., et al. 2008, *MNRAS*, 386, 1464.
doi:10.1111/j.1365-2966.2008.13128.x
- Rauw, G., & Nazé, Y. 2016, *Advances in Space Research*, 58, 761

- Riaz, B., Gizis, J. E., & Harvin, J. 2006, *AJ*, 132, 866. doi:10.1086/505632
- Russell, S. C. & Dopita, M. A. 1990, *ApJS*, 74, 93. doi:10.1086/191494
- Sabbi, E., Anderson, J., Lennon, D. J., et al. 2013, *AJ*, 146, 53. doi:10.1088/0004-6256/146/3/53
- Sabbi, E., Lennon, D. J., Anderson, J., et al. 2016, *ApJS*, 222, 11
- Sartore, N., Ripamonti, E., Treves, A., et al. 2010, *A&A*, 510, A23. doi:10.1051/0004-6361/200912222
- Schnurr, O., Moffat, A. F. J., Villar-Sbaffi, A., et al. 2009, *MNRAS*, 395, 823
- Shenar, T., Sana, H., Marchant, P., et al. 2021, *A&A*, 650, A147. doi:10.1051/0004-6361/202140693
- Shenar, T., Richardson, N. D., Sablowski, D. P., et al. 2017, *A&A*, 598, A85
- Skrutskie, M. F., Cutri, R. M., Stiening, R., et al. 2006, *AJ*, 131, 1163
- Smith, R. K., & Hughes, J. P. 2010, *ApJ*, 718, 583
- Sota, A., Maíz Apellániz, J., Walborn, N. R., et al. 2011, *ApJS*, 193, 24
- Sota, A., Maíz Apellániz, J., Morrell, N. I., et al. 2014, *ApJS*, 211, 10
- Taylor, M. B. 2005, in *ASP Conf. Ser.* 347, *Astronomical Data Analysis Software and Systems XIV*, ed. P. Shopbell, M. Britton, & R. Ebert (San Francisco, CA: ASP), 29
- Taylor, W. D., Evans, C. J., Sana, H., et al. 2011, *A&A*, 530, L10. doi:10.1051/0004-6361/201116785
- Tehrani, K. 2019, dissertation “Wolf-Rayet Populations in Local Group Metal Poor Galaxies”, University of Sheffield
- Townsley, L. K., Feigelson, E. D., Montmerle, T., et al. 2003, *ApJ*, 593, 874
- Townsley, L. K., Broos, P. S., Feigelson, E. D., Brandl, B. R., Chu, Y.-H., Garmire, G. P., & Pavlov, G. G. 2006a, *AJ*, 131, 2140
- Townsley, L. K., Broos, P. S., Feigelson, E. D., Garmire, G. P., & Getman, K. V. 2006b, *AJ*, 131, 2164
- Townsley, L. K., Broos, P. S., Corcoran, M. F., et al. 2011, *ApJS*, 194, 1
- Townsley, L. K., Broos, P. S., Chu, Y.-H., et al. 2011, *ApJS*, 194, 15
- Townsley, L. K., Broos, P. S., Chu, Y.-H., et al. 2011, *ApJS*, 194, 16
- Townsley, L. K., Broos, P. S., Garmire, G. P., et al. 2014, *ApJS*, 213, 1 (MOXC1)
- Townsley, L. K., & Broos, P. S. 2017, MOXC2 data products, Zenodo, doi:10.5281/zenodo.1067749
- Townsley, L. K., Broos, P. S., Garmire, G. P., et al. 2018, *ApJS*, 235, 43 (MOXC2)
- Townsley, L. K., & Broos, P. S. 2023, T-ReX data products, Zenodo, 10.5281/zenodo.8388113
- Townsley, L. K., Broos, P. S., Garmire, G. P., & Povich, M. S. 2019, *ApJS*, 244, 28 (MOXC3)
- Uchida, H., Katsuda, S., Tsunemi, H., et al. 2019, *ApJ*, 871, 234. doi:10.3847/1538-4357/aaf8a6
- Vink, J. S. & de Koter, A. 2005, *A&A*, 442, 587. doi:10.1051/0004-6361:20052862
- Vuong, M. H., Montmerle, T., Grosso, N., et al. 2003, *A&A*, 408, 581
- Walborn, N. R. & Blades, J. C. 1997, *ApJS*, 112, 457. doi:10.1086/313043
- Walborn, N. R., Barbá, R. H., & Sewilo, M. M. 2013, *AJ*, 145, 98. doi:10.1088/0004-6256/145/4/98
- Walborn, N. R., Sana, H., Simón-Díaz, S., et al. 2014, *A&A*, 564, A40. doi:10.1051/0004-6361/201323082
- Wang, Q. D., Gotthelf, E. V., Chu, Y.-H., et al. 2001, *ApJ*, 559, 275. doi:10.1086/322392
- Watson, C., Povich, M. S., Churchwell, E. B., et al. 2008, *ApJ*, 681, 1341. doi:10.1086/588005
- Weiskopf, M. C., Wu, K., Trimble, V., et al. 2007, *ApJ*, 657, 1026
- Whitney, B. A., Sewilo, M., Indebetouw, R., et al. 2008, *AJ*, 136, 18. doi:10.1088/0004-6256/136/1/18
- Wilms, J., Allen, A., & McCray, R. 2000, *ApJ*, 542, 914
- Zhang, S., Wang, Q. D., Sun, W., et al. 2022, *ApJ*, 941, 68. doi:10.3847/1538-4357/aca01a